

Optics-free spatial genomics for mapping mammalian brain aging by IRISeq

Received: 5 April 2025

Accepted: 6 April 2026

Published online: 12 May 2026


 Check for updates

Abdulraouf Abdulraouf^{1,2,3,4}, Weirong Jiang^{1,4}, Zehao Zhang^{1,3}, Zihan Xu^{1,3}, Ziyu Lu^{1,3}, Tiffany Merlinsky², Andrew Liao^{1,2,3}, Ahmet Doymaz^{1,2,3}, Samuel Isakov¹, Tanvir Raihan¹, Wei Zhou^{1,5}  & Junyue Cao^{1,5} 

Spatial transcriptomics has emerged as a transformative approach for in situ mapping of cellular heterogeneity and interactions, yet existing methods often compromise throughput, cost and tissue coverage. Here we introduce Imaging Reconstruction using Indexed Sequencing (IRISeq): an optics-free, cost-effective platform that leverages spatial interaction mapping by indexed sequencing to profile tissues at adjustable sizes and resolutions (5–50 μm). We applied IRISeq to map gene expression across more than 70 coronal sections from both adult and aged mouse brains, including wild-type and two lymphocyte-deficient models (*Rag1* and *Prkdc* mutants) and generated more than 460,000 spatial transcriptome profiles. Our integrated analysis with 783,264 single-cell transcriptomes revealed region-specific aging signatures that are lymphocyte dependent, notably a downregulation of interferon signaling and inflammation in ventricular regions upon lymphocyte depletion, alongside mutant-specific upregulation of senescence pathways. Furthermore, lymphocyte deficiency was linked to preserved abundance of ependymal cells that line the brain's ventricles and to distinct microglial state dynamics, highlighting a key role for lymphocytes in driving inflammatory processes during brain aging. Overall, IRISeq provides a high-throughput and cost-effective solution for spatially resolved transcriptomic profiling, opening new avenues for elucidating region-specific cellular mechanisms underlying aging and identifying potential therapeutic targets to preserve brain homeostasis.

Understanding the spatial organization of molecules and cells is essential for studying cellular network dynamics in aging and disease. Although recent advances in spatial transcriptomics, such as multiplexed in situ hybridization^{1–3} and indexed oligonucleotide capture arrays^{4–10}, have greatly expanded our ability to profile genome-wide RNA expression across anatomical locations, current methods still face limitations in throughput, cost and comprehensive tissue coverage. Specifically, methods like in situ hybridization are limited by

imaging speed, and indexed array methods (for example, 10x Visium, Slide-seq^{5,11}) are often constrained by scalability, area coverage or the technical challenges of optical imaging. The concept of 'spatial mapping by sequencing' uses barcoded DNA sequences to encode spatial proximity among biological molecules¹². This strategy, first used in DNA Hi-C to reconstruct three-dimensional chromatin structure¹³, has recently been adapted to measure spatial interactions among targeted messenger RNAs (mRNAs) in cultured cells¹⁴ and the

¹Laboratory of Single Cell Genomics and Population Dynamics, The Rockefeller University, New York, NY, USA. ²The Tri-Institutional M.D-Ph.D Program, New York, NY, USA. ³The David Rockefeller Graduate Program in Bioscience, The Rockefeller University, New York, NY, USA. ⁴These authors contributed equally: Abdulraouf Abdulraouf, Weirong Jiang. ⁵These authors jointly supervised this work: Wei Zhou, Junyue Cao.  e-mail: wzhou@rockefeller.edu; jcao@rockefeller.edu

distribution of cellular surface proteins¹⁵. Despite these advances, a robust, high-throughput and cost-effective sequencing-based platform for region-specific transcriptomic analysis of complex tissues remains unavailable.

Here we present Imaging Reconstruction using Indexed Sequencing (IRISeg), a scalable and cost-effective spatial genomic method that relies entirely on sequencing, eliminating the need for predefined capture arrays or optical imaging. IRISeg uses DNA-barcoded beads to capture gene expression across thousands of spatial locations and infers bead positions from interaction signals with neighboring beads. We applied IRISeg to adult and aged mouse brain sections and identified both widespread and region-specific molecular and cellular changes in aging. By integrating IRISeg with our single-nucleus genomics platform EasySci¹⁶, we further showed that depleting functional lymphocytes reduces IFN-responsive glial populations and preserves ependymal cells in aged ventricles.

Results

Overview of IRISeg

The optimized IRISeg protocol involves several key steps (Fig. 1a–c). First, two types of oligo-barcoded beads are prepared: receiver beads coated with poly(T) sequences to capture nearby cellular mRNA and sender beads carrying a photocleavable linker and poly(A) sequence. These beads are generated through a split-pool ligation approach¹⁷ so that each bead carries a unique barcode. Second, the beads are evenly distributed on a glass slide, and ultraviolet exposure allows local diffusion and capture of sender oligos by nearby receiver beads, mimicking the capture of tissue mRNA. Third, frozen tissue sections are transferred onto the array, and tissue mRNA is captured by receiver beads through hybridization and tissue digestion. Fourth, after tissue digestion, beads are collected for reverse transcription (RT), second-strand synthesis, tagmentation and polymerase chain reaction (PCR), followed by sequencing to generate transcriptome and bead-connection information. Detailed IRISeg protocols are provided to enable cost-efficient spatial transcriptomic mapping of tissue sections in individual laboratories (Supplementary Note 1 and Supplementary Table 1).

After library preparation and sequencing, IRISeg yields two outputs: a bead–bead interaction matrix for identifying connections and a gene expression matrix assigning transcripts to each receiver bead (Fig. 1e, left). The global spatial positions of receiver beads were inferred by applying principal component analysis (PCA) and uniform manifold approximation and projection (UMAP)¹⁸ to the interaction matrix (Methods and Extended Data Fig. 1). The resulting two-dimensional UMAP coordinates recapitulated the designed assay layout and preserved positional relationships among beads (Fig. 1e, middle). Simultaneously, the gene expression matrix was used for dimensionality reduction and clustering to annotate receiver beads based on region-specific expression patterns (Fig. 1e, right).

For an initial demonstration, we used a 50- μ m bead array (0.6 cm \times 0.6 cm) to profile a coronal mouse brain section (Fig. 1f). This experiment yielded 5,028 receiver beads, each capturing a median of 4,587 unique transcripts (2,535 genes) and 1,998 unique bead–bead connection oligos, with each receiver bead connecting to a median of five sender beads (Fig. 1g and Extended Data Fig. 2a). Clustering analysis of receiver-bead gene expression profiles identified 12 transcriptionally distinct brain region clusters, validated by region-specific markers (Fig. 1i) and external datasets (Extended Data Fig. 2b–d). We then reconstructed the spatial positions of all receiver beads using only their connection signals with sender beads (Fig. 1h). The resulting image preserved local neighborhood structure and accurately positioned beads from distinct brain regions in their expected locations, similar to the preindexed 10x Visium oligo array (Fig. 1j and Extended Data Fig. 2e,f). Of note, although UMAP replicates may differ slightly in overall orientation or global placement, the relative distances and local relationships

between beads remained highly stable, confirming the reproducibility of spatial reconstruction (Extended Data Fig. 2g). Overall, these results demonstrate that IRISeg can map spatially barcoded transcriptomes without optical imaging.

A distinctive feature of IRISeg is its ability to reconstruct bead positions solely from local interactions, eliminating the need for preindexed arrays or imaging. This enables profiling of large tissue sections beyond the limits of conventional methods, demonstrated by the simultaneous profiling of two entire mouse brain sections on a 1.5 cm \times 1.5 cm array (Extended Data Fig. 2h–k). Furthermore, its generalizability was shown by successfully profiling a high-resolution (10- μ m) mouse kidney section. At only 20% sequencing saturation, we captured a median of 1,306 unique molecular identifier (UMI) counts and 882 unique genes (Extended Data Fig. 2l). Analysis resolved expected renal territories, and canonical markers showed the expected spatial patterns (Extended Data Fig. 2m–s). In addition, IRISeg offers adjustable resolution by varying bead size, similar to other bead-based spatial transcriptomics methods^{5,11}. To support high-resolution profiling, a dendrimer-based strategy¹⁹ was implemented during bead synthesis, which markedly increased oligo density on the bead surface (Fig. 2a and Extended Data Fig. 3a).

We next evaluated the performance of high-resolution IRISeg using 10- μ m and 5- μ m beads. A 0.6-cm diameter circular bead array with 10- μ m beads yielded 384,802 unique receiver beads before quality filtering and 78,791 high-quality receiver beads from a mouse hippocampal section (Fig. 2b). Despite relatively shallow sequencing depth (63% saturation), we achieved a mean capture of 926 UMIs and 646 genes per receiver bead, with medians of 763 UMIs and 558 genes (Extended Data Fig. 3b–d). Using an annotated single-cell reference from the mouse brain²⁰, we assigned cell identities to bead-specific transcriptomes from the high-density array (Fig. 2c and Methods). The identified diverse brain cell types mapped to their expected anatomical locations (Extended Data Fig. 3e) and were further validated by region-specific gene expression patterns, such as *C1ql2* in the dentate gyrus (Fig. 2d). We further validated the approach in a cerebellum section, where we observed highly specific spatial localization of cerebellar granule neurons and Purkinje neurons (Fig. 2e–g and Extended Data Fig. 3f). Testing with 5- μ m beads, we achieved an even higher density of 154,103 high-quality beads (an average of 404 UMIs and 309 genes per bead) for detailed mapping of gene expression in the hippocampal section, including *Trt* in the ventricles and *Hpca* in the hippocampus (Extended Data Fig. 3g). Notably, the practical resolution of IRISeg corresponds directly to bead diameter, and transcript capture efficiency remains robust relative to existing high-resolution methods under comparable conditions.

In summary, IRISeg offers several key advantages over traditional spatial genomic methods: it is more cost-effective than typical commercial platforms²¹ (approximately \$30 per tissue section; Fig. 1d); scalable for profiling multiple, large tissue sections; and enables optics-free spatial mapping via local neighborhood interactions. Furthermore, its adjustable resolution through varying bead size establishes IRISeg as a versatile platform for spatial transcriptomic analysis across diverse research applications.

A spatially resolved transcriptome atlas of the mouse brain

We utilized IRISeg to profile 24 coronal sections from adult (4-month) and aged (23-month) wild-type (WT) C57BL/6 mouse brains ($n = 3$ per age group), spanning the frontal to dorsal cortex, including the hippocampus, thalamus, hypothalamus and surrounding regions. For each brain, this included one frontal cortex section ('section 1'), one middle cortex section ('section 2') and two adjacent dorsal cortex sections ('section 3') (Fig. 3a). After processing and quality control, we recovered a median of 3,905 receiver beads per section, yielding 98,006 spatially distinct transcriptome profiles overall (Fig. 3b). Although these samples were generated using an earlier version of

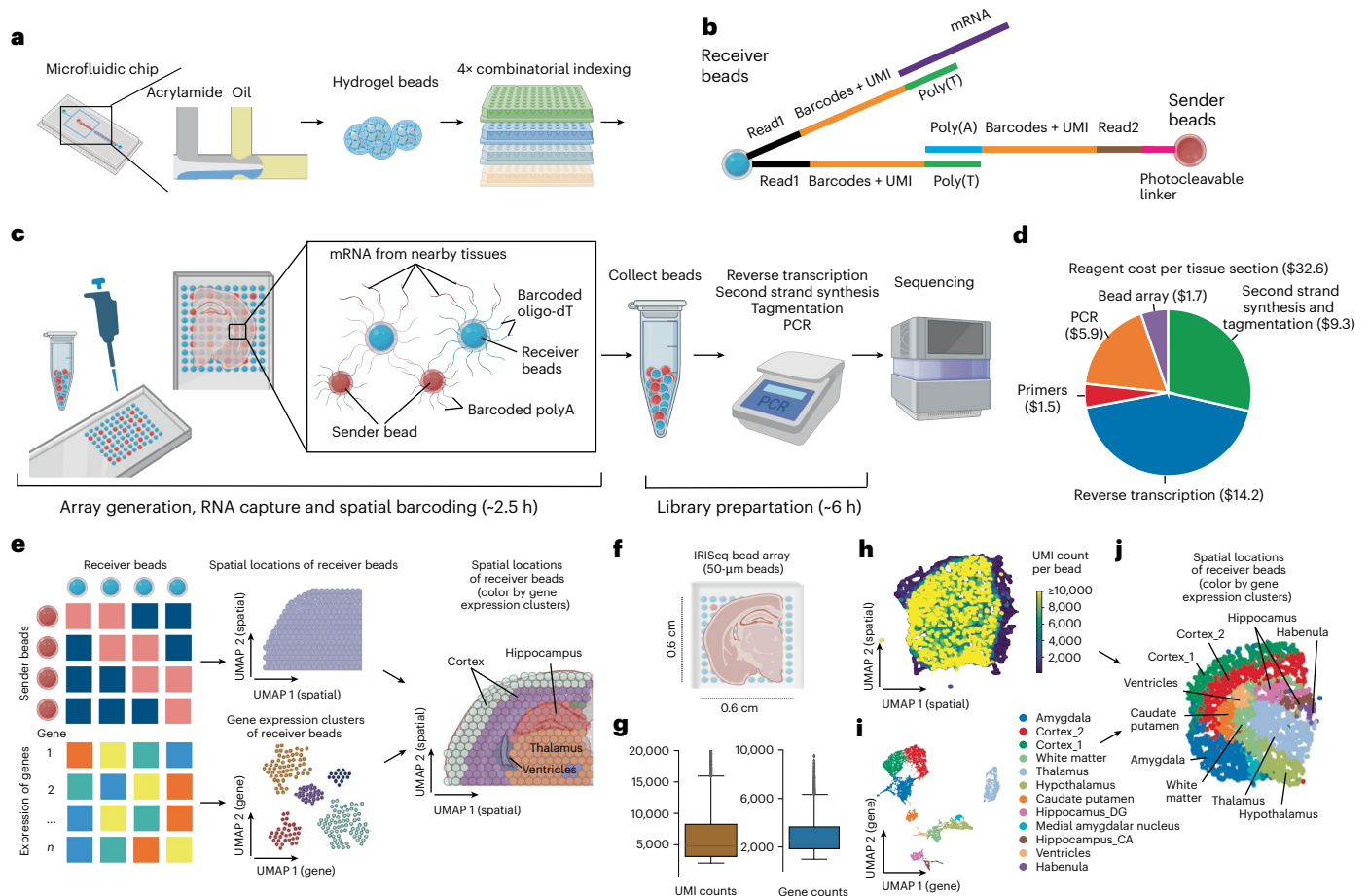


Fig. 1 | Overview and validation of the IRISec platform. **a**, Schematic illustrating the generation of barcoded hydrogel beads ('sender beads' and 'receiver beads') through combinatorial indexing. **b**, Diagram showing the dual interaction between sender and receiver beads for capturing RNA from tissue samples and indexing spatial locations on the array. **c**, Schematic illustrating the IRISec experimental pipeline utilizing barcoded gel beads ('receiver beads') to capture mRNA expression from nearby cells, along with barcoded oligos from adjacent 'sender beads' for spatial localization. **d**, Pie chart detailing the reagent cost breakdown for profiling a tissue section using a 0.6 cm × 0.6 cm bead array. **e**, Diagram showing the generation of gene count and bead–bead connection matrices from IRISec data to identify region-specific gene expression and infer bead spatial locations for image reconstruction. **f**, Depiction of a small-scale IRISec experiment using a 0.6 cm × 0.6 cm bead array to profile a mouse brain

hemisection. **g**, Box plots displaying the distribution of unique transcripts and gene counts across 5,028 receiver beads from a single tissue section ($n = 5,028$ observations from one section). Center line, median; box, interquartile range; whiskers, minimum to maximum. **h**, UMAP plot showing the spatial distribution of receiver beads based on interactions with sender beads, colored by the number of unique transcripts per bead. **i**, We integrated the gene expression data of receiver beads with spatial transcriptome data from 10x Visium¹⁶. The UMAP plot shows the integrated gene expression clusters, with each bead colored by annotated brain regions. **j**, UMAP plot visualizing the spatial distribution of receiver beads, with each bead colored by annotated brain regions. Schematics created in BioRender: **a**, Cao, J. <https://biorender.com/6cr9gte> (2026); **b,c,e,f**, Cao, J. <https://biorender.com/i2ew4vq> (2026).

IRISec that was less efficient than the optimized platform (Supplementary Note 1), we still recovered an average of 3,725 unique transcripts and 6,771 unique bead–bead connection oligos per receiver bead (Extended Data Fig. 4a–c).

To annotate spatial transcriptomic profiles across brain regions, we integrated IRISec gene expression data with published datasets from corresponding brain sections using LIGER^{22,23,24}. This analysis showed strong overlap with published datasets and enabled annotation of 25 distinct brain regions (Extended Data Fig. 4d). Spatial location was then reconstructed using bead–bead connection information. These reconstructions were highly consistent with both gene expression-based annotations and published references (Fig. 3d and Extended Data Fig. 4e), an accuracy further supported by region-specific marker genes (for example, *Tac1* and *Ttr*) (Fig. 3e). Cross-replicate correlation analysis also demonstrated reproducible spatial transcriptomic profiles across tissue sections (Extended Data Fig. 5). To define spatial cell-type organization, we applied robust cell-type decomposition

(RCTD)²⁵ to integrate the spatial transcriptomics data from IRISec with our previously published brain single-cell transcriptome dataset that has identified more than 300 distinct cell subtypes across different age stages¹⁶. This effectively mapped known brain cell types and subtypes across various regions (Extended Data Fig. 4f), and the inferred cell-type locations showed high concordance with an independent 10x Visium platform¹⁶ (Extended Data Fig. 6).

We next identified highly region-specific gene features and cell types through differential analysis (Extended Data Fig. 4g and Supplementary Tables 3 and 4). For instance, genes like *Ccdc153* and *Rarres2* were highly enriched in the ventricular areas of sections 2 and 3, consistent with previous findings^{26,27} (Fig. 3b). However, section-specific features were also evident, such as the enriched expression of *Enpp2* only in section 3. Similarly, cell-type distributions varied by section and region; specific choroid plexus subtypes (for example, *ChPec-2*, *ChPec-4*) enrichment mainly appeared in section 3, corresponding with its prevalence near the ventricle regions.

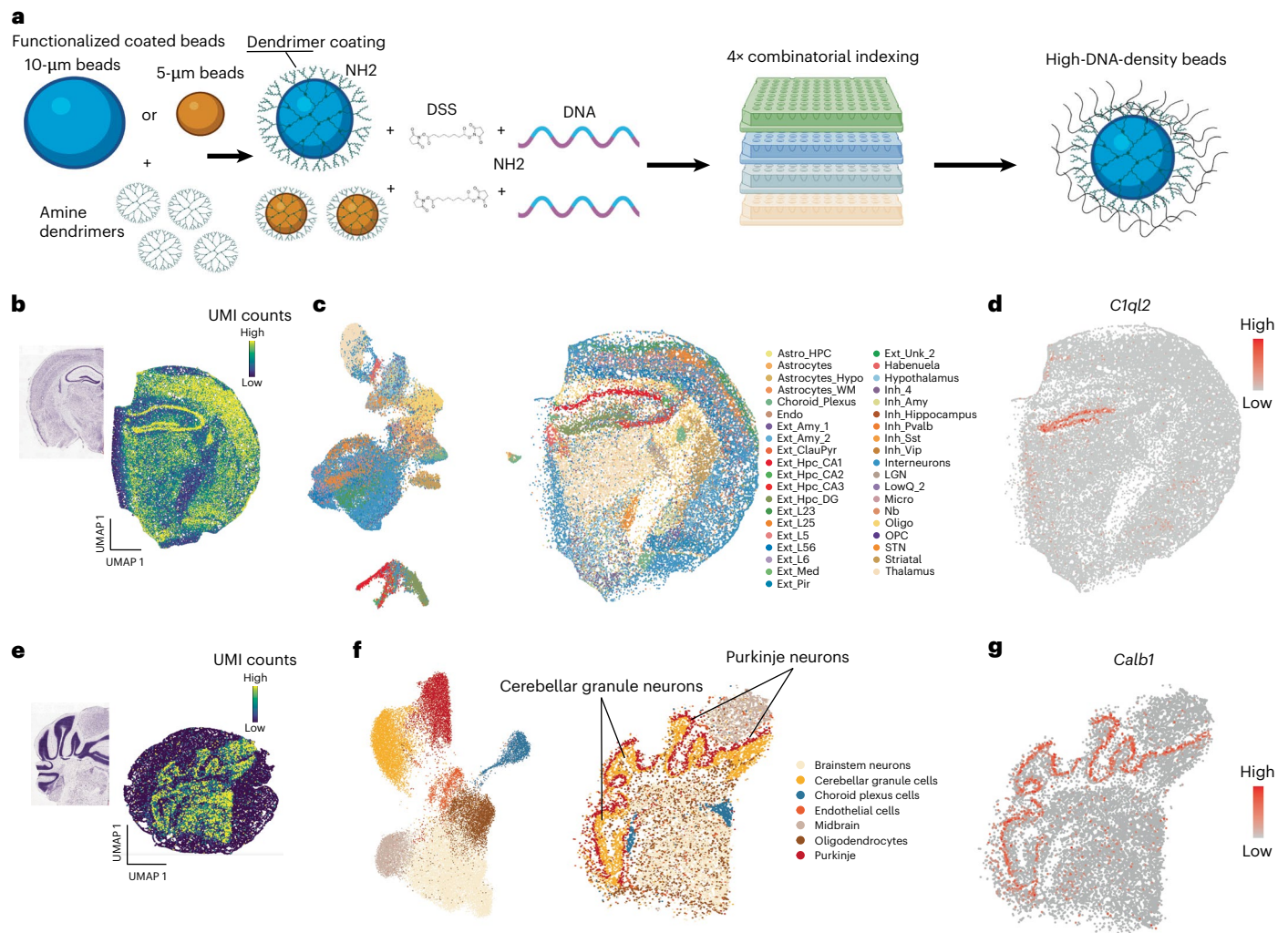


Fig. 2 | High-resolution spatial transcriptomics profiling enabled by the IRISeq platform. **a**, Schematic illustrating the dendrimer-based strategy for generating high-DNA-density beads. Functionalized beads are incubated with poly(amidoamine) dendrimers. DNA primers are then conjugated to the beads, followed by split-pool bead barcoding. **b**, Analysis of a mouse brain tissue section encompassing the hippocampal region, with UMI density mapped onto the spatially reconstructed array. **c**, Gene expression UMAP overlaid on the spatial reconstruction, revealing clusters aligned with known anatomical features. **d**, Expression plot of *C1ql2*, a marker specific to the dentate gyrus. **e**, Spatial profiling of the mouse hindbrain region, showing UMI density distributions and anatomical boundaries. **f**, Gene expression UMAP overlaid on the spatial reconstruction, highlighting clusters corresponding to distinct anatomical structures. **g**, Visualization of *Calb1*, a Purkinje cell marker, demonstrating its

specificity to the Purkinje cell layer. Schematic in **a** created in BioRender; Abdul, A. <https://biorender.com/ncdwr0r> (2026); Cao, J. <https://biorender.com/6cr9gte> (2026). Chemical structure of DSS reproduced from Wikimedia Commons (Edgar181, public domain). Histology images in **b, e** reproduced from Allen Brain Atlas⁵⁰. Astro, astrocytes; Amy, amygdala; CA1–CA3, hippocampal cornu ammonis regions 1–3; ClauPyr, claustrum/piriform cortex; DG, dentate gyrus; DSS, disuccinimidyl suberate; Endo, endothelial cells; Ext, excitatory neurons; HPC, hippocampus; Hypo, hypothalamus; Inh, inhibitory neurons; LGN, lateral geniculate nucleus; LowQ, low-quality cluster; Micro, microglia; Nb, neuroblasts; Oligo, oligodendrocytes; OPC, oligodendrocyte precursor cells; Pvalb, parvalbumin-positive interneurons; Sst, somatostatin-positive interneurons; STN, subthalamic nucleus; Unk, unknown cluster; Vip, vasoactive intestinal peptide-positive interneurons; WM, white matter.

Age-associated changes in region-specific gene expression programs

We next investigated aging-associated gene expression changes by conducting differentially expressed gene (DEG) analysis across 25 brain regions, identifying 538 unique upregulated genes and 386 unique downregulated genes (false discovery rate (FDR) of 0.05, with more than threefold changes between aged and young brains) (Fig. 4a and Supplementary Table 5). Among these, 80 downregulated and 33 upregulated genes consistently exhibited aging-associated changes in more than ten brain regions (Fig. 4b). Genes showing global downregulation were primarily associated with mitochondrial function (for example, *Cox8a*, *Cox17*), ribosomal functions (for example, *Rpl30*, *Rps15a*) and cilia functions (for example, *Cfap74*, *Catsperd*) (Extended Data Fig. 7a). These findings suggest age-related declines in energy production,

cellular metabolism, protein synthesis and ependymal cell function^{28,29}, which may impair ciliary performance and fluid circulation in the aging brain³⁰ (Fig. 4b).

In contrast, genes upregulated across aged brain regions were significantly enriched in immune-response pathways, including the complement pathway, antigen presentation and interferon response (Fig. 4b and Extended Data Fig. 7a). Although broadly altered, the greatest changes in interferon response occurred in the ventricular regions, a primary site of inflammation in brain aging²⁸ (Fig. 4c,d). These regional changes were accompanied by the downregulation of neurogenesis genes (for example, *Hdac8*, *Romo1*) and upregulation of genes related to glial activation (for example, *Serpina3n*, *Gfap*), findings consistently confirmed across different ventricular regions in two coronal sections (Extended Data Fig. 7b,c). Reanalysis of a previously published dataset¹⁶

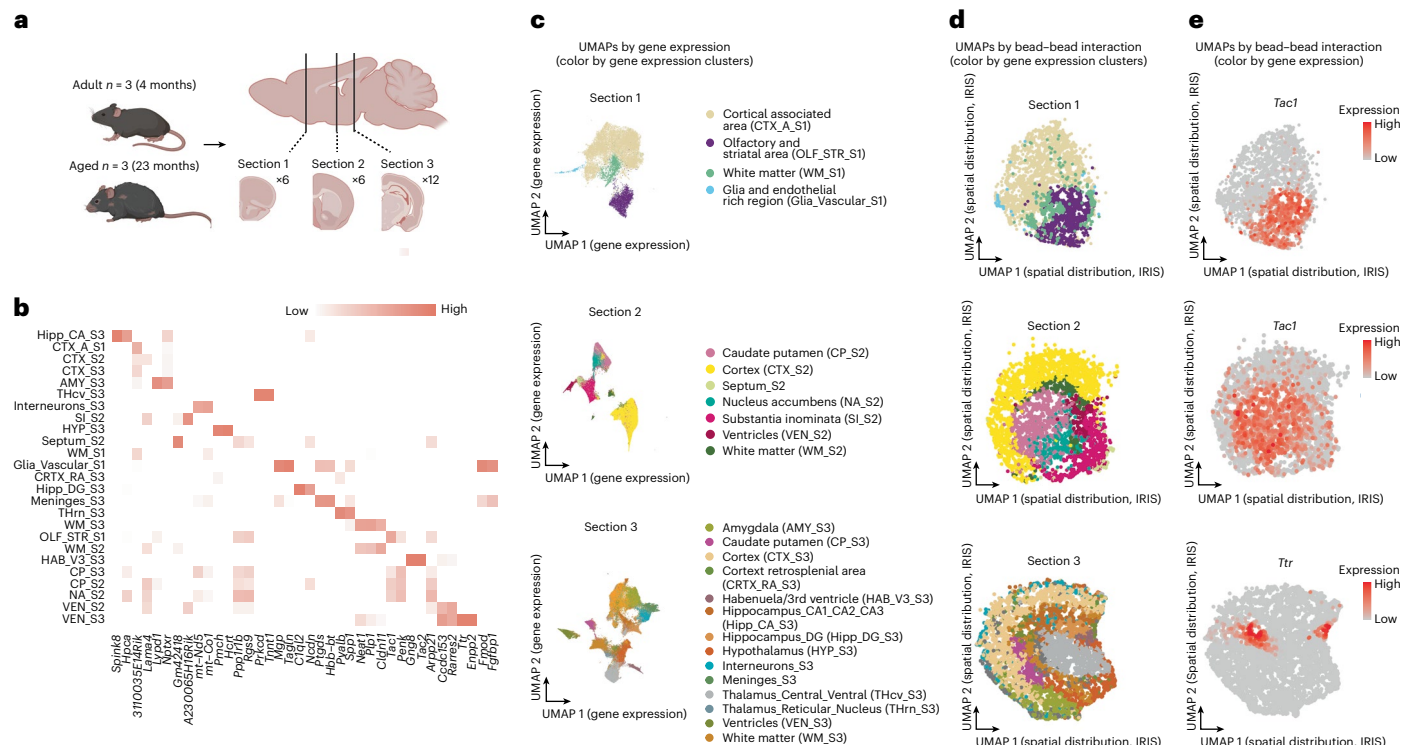


Fig. 3 | Spatial transcriptomic analysis of mouse brain aging using IRISeq. **a**, Schematic of IRISeq profiling across various brain regions, including the frontal isocortex, dorsal cortex, hippocampus, thalamus, hypothalamus and additional associated regions. ‘Section 1’ and ‘section 2’ are for the frontal and middle parts of the cortex, and ‘section 3’ is near the dorsal part of the cortex. **b**, Regional gene expression heatmap. **c**, Regional gene expression UMAP. **d,e**, Image reconstruction of all receiver beads derived from bead–bead connections (**d**), with coloring corresponding to the annotated regions based on gene expression (**e**). Schematic in **a** created in BioRender; Cao, J.

<https://biorender.com/c6n61lz> (2026). AMY, amygdala; CA1–CA3, hippocampal cornu ammonis regions 1–3; CP, caudate putamen; CRTX_RA, retrosplenial cortical area; CTX, cortex/cortical area; CTX_A, cortical associated area; DG, dentate gyrus; Glia_Vascular, glia- and endothelial-rich region; HAB_V3, habenula/third ventricle region; HYP_CA, hippocampal CA1–CA3 region; Hipp_DG, hippocampal dentate gyrus; HYP, hypothalamus; NA, nucleus accumbens; OLF_STR, olfactory and striatal area; SI, substantia innominata; THcv, central ventral thalamus; THrn, thalamic reticular nucleus; VEN, ventricles; V3, third ventricle; WM, white matter. S1–S3 indicate tissue sections 1–3, respectively.

further detected increased interferon-associated gene expression in ependymal cells, underscoring enhanced interferon responses in the ventricles and ventricle-associated cells (Extended Data Fig. 7d).

Meanwhile, some aging-associated expression changes are region-specific (Fig. 4b). In several brain areas, downregulated genes are primarily neuronal markers involved in signaling and transcriptional regulation (for example, *Pvalb*, *Cck*, *Sst*), suggesting age-related neuronal loss. Additionally, smooth-muscle-related genes (for example, *Myom1*, *Mylk*, *Myl9*) were significantly downregulated in aged brain vascular regions, indicating declining vascular integrity with age (Extended Data Fig. 7e). Conversely, region-specific upregulation includes lymphocyte markers (for example, *Cd24a*, *Ighm* and *Cd52*), particularly in the ventricles, white matter and hypothalamus (Extended Data Fig. 7f,g). Other findings included a fivefold increase in *Sult1c1* in the aged ventricular region of section 3, unique upregulation of *Clec18a* in the aged habenular region and a decrease in *Hprt* in the aged hypothalamic region. The observed age-related, region-specific gene expression changes were further validated using the 10x Visium platform¹⁶ (Extended Data Fig. 7h).

Age-associated changes in the spatial distribution and interaction of different cell types

Using the cell-type-specific deconvolution approach RCTD²⁵ to integrate IRISeq spatial expression data with a published single-cell transcriptome dataset¹⁶, we mapped previously annotated brain cell types and subtypes across various regions. We then conducted differential abundance analyses to explore region-specific cell population dynamics during aging and quantified cell–cell interactions by

analyzing colocations on the same bead (Fig. 5a). Using differential abundance analysis between adult and aged conditions, we identified 123 region-specific differentially abundant cellular subtypes (twofold change between ages with an FDR of 0.05) (Fig. 5b,c and Supplementary Table 6). The high consistency between these results and previously published dataset¹⁶ validated the reliability of our deconvolution and regional abundance analysis (Fig. 5d).

Compared to single-cell analysis, spatial transcriptome analysis offers unique advantages for identifying region-specific cell population alterations in the aged brain. The most depleted populations in the aged brain included olfactory bulb (Ob) neuroblasts (marked by *Prokr2* and *Robo2*) and Ob neuronal progenitor cells (marked by *Mki67* and *Egfr*³¹), found primarily in the ventricle regions, which aligns with reduced adult neurogenesis along the walls of the lateral ventricles³² (Fig. 5c). Additionally, various vascular and blood cell types, including *Myh11*+ vascular smooth-muscle cells and *Nefh*+ endothelial cells, were significantly depleted, indicating region-specific dysregulation of the vascular system in aging³³. Furthermore, a specific ependymal cell subtype (*Slit2*+) was depleted in the ventricles, corroborating global single-cell analysis and suggesting impaired cerebrospinal fluid flow in the aged brains³⁴ (Fig. 5c,d).

Meanwhile, several cell subtypes significantly expanded across different regions in the aged brain (Fig. 5c,d). For example, the ventricular and meningeal regions in section 3 showed the highest predicted lymphocyte abundance with aging (Extended Data Fig. 7g). Other significantly expanded cell types included disease-associated microglia (DAM, marked by *Apoe*+, *Csf1*+) and a reactive oligodendrocyte subtype (OLG-7, *C4b*+, *Serpina3n*+ (refs. 35,36)), both predominantly found in

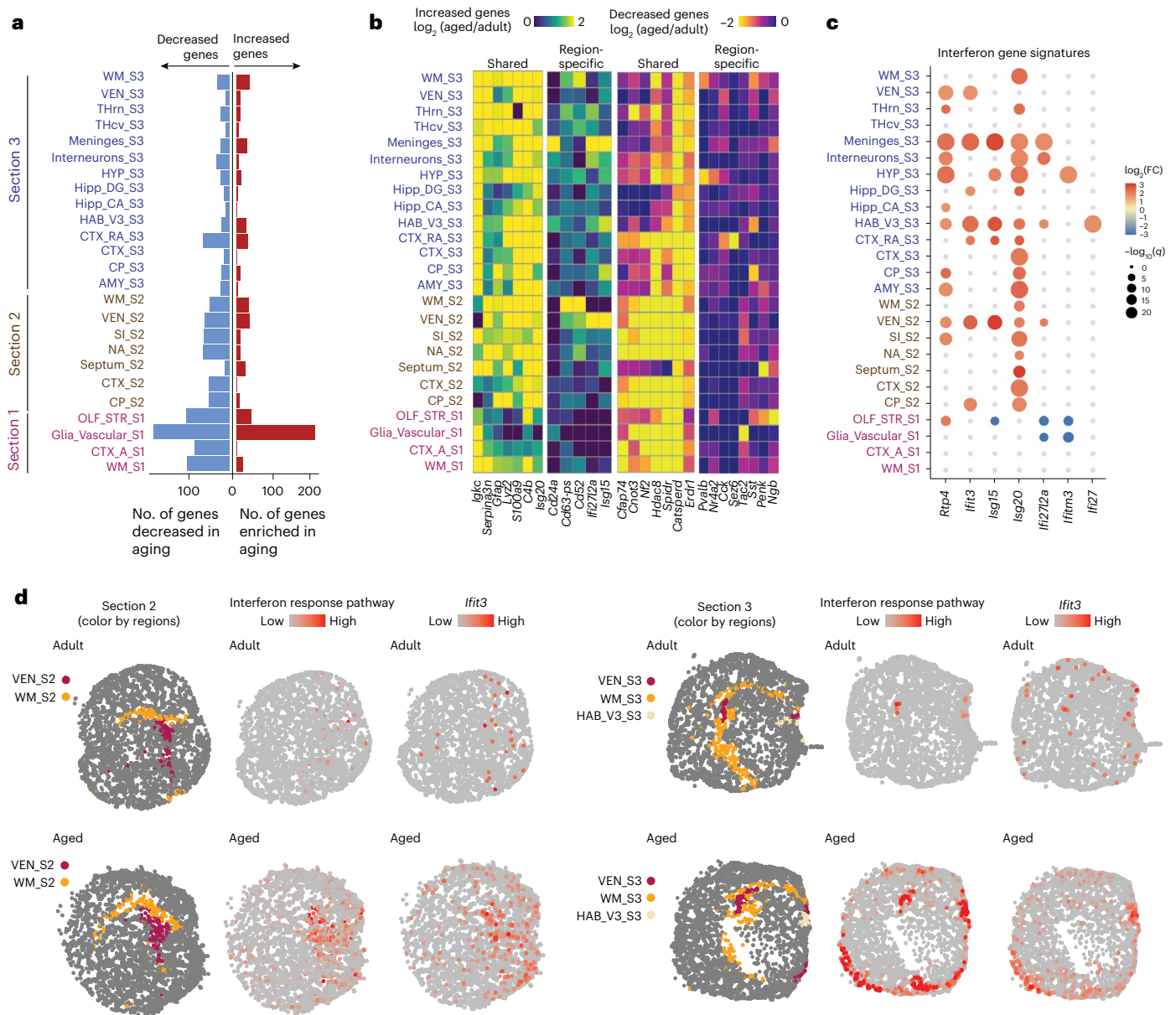


Fig. 4 | Age-associated changes in region-specific gene expression programs. **a**, Bar charts depict the number of genes DE between adult and aged animals across various brain regions, categorized as upregulated (red) and downregulated (blue). DE genes are defined by more than threefold changes between the ages with an FDR-adjusted P value < 0.05 . Numbers of significant genes were calculated from region-specific DE analysis for aging using the likelihood-ratio test in Monocle2; q -values denote multiple-testing-adjusted P values. Significant genes were defined as those with $q < 0.05$, $FC > 3$ between the highest and second-highest expressed conditions and $TPM > 50$ in the highest expressed condition. **b**, Heatmap showing the \log_2 -transformed FCs in normalized gene expression between aged and adult animals for DE genes across

different brain regions, distinguishing shared changes (left) from region-specific changes (right). **c**, Barplots showing the scaled expression and standard error of gene modules related to interferon response across brain regions in both adult (blue) and aged (red) conditions. Gene inclusion for interferon module (*Ifi27*, *Ifitm3*, *Ifi27l2a*, *Isg20*, *Isg15*, *Ifit3*, *Rtp4*) (b). Expression values for each pathway were calculated by aggregating and normalizing pathway-related gene expressions, followed by log transformation and scaling. **d**, Reconstructed spatial maps display the expression levels of gene modules associated with the complement and interferon response pathways in adults (top) and aged animals (bottom) for sections 2 (left) and 3 (right).

the white-matter and ventricle regions and validated by the 10x Visium dataset¹⁶. This expansion aligns with the notably upregulated inflammatory response in these areas (Fig. 4d). Furthermore, border-associated macrophages (marked by *Mrc1*, *Cd163* and *Lyz2*) expanded around the meningeal and white-matter regions (Fig. 5c,d), a change reported to contribute to age-related vascular function defects^{37,38}.

Leveraging the IRISeq platform, where each bead captures transcriptomes from multiple cells within the same neighborhood, we quantified colocalization of two cell subtypes around the same beads to assess local cellular spatial interactions (Methods). Differential

analysis identified a total of 499 interaction pairs significantly altered with aging (1.5-fold change between ages, with an FDR of 1×10^{-5}), prominently in cortical, striatal, amygdala and white-matter regions (Fig. 5f,g and Supplementary Table 7). Although most changes were region-specific, aged white matter showed a consistent decrease in interactions between *Pcdh6*+ oligodendrocyte precursor cells (OLG-6) and *Gfap*-low *Fat2*-high astrocytes (Astrocyte-12) across different sections (Fig. 5f), corresponding with reduced abundance of oligodendrocyte differentiation during aging¹⁶. Conversely, we noted increased colocalization among *Csf1*+ disease-associated microglia

(DAM), *C4b*+ reactive oligodendrocytes and *Gfap*-high activated astrocytes, which are involved in astroglial activation and gliosis during aging and neurodegeneration³⁹ (Fig. 5f,g). This upregulated colocalization, which we termed a potential ‘DAM niche’, was further validated by 10x Visium (Extended Data Fig. 8d). A hypergeometric test confirmed that interactions between reactive oligodendrocytes, DAM and activated astrocytes were significantly enriched within the same neighborhood, beyond what is expected from random distribution (P values = 0.0005 and 1×10^{-17} for interactions between DAM and reactive oligodendrocytes and between DAM and activated astrocytes) (Fig. 5h and Extended Data Fig. 9). Gene signature analysis of the ‘DAM niche’ beads further supported these altered cellular interaction networks as key features of brain aging (Fig. 5i and Extended Data Fig. 8f).

Unraveling lymphocyte-driven mechanisms in mouse brain aging

Recent studies⁴⁰ indicate that T cells, particularly CD4+ subsets, infiltrate the central nervous system in neurodegenerative diseases like Lewy body dementia and Alzheimer’s disease, contributing to neuronal damage. Aligning with these reports, we observed a dramatic increase in lymphocyte-associated signaling (for example, *Cd24a*, *Ighm* and *Cd52*) across different brain regions associated with aging (Fig. 4b). To further investigate the role of lymphocytes in brain aging, we employed a systemic lymphocyte knockdown strategy using two immunodeficient mouse genotypes—*B6.129S7-Rag1tm1Mom/J* and *B6.Cg-Prkdcscid/SzJ*—that lack functional or mature lymphocytes^{41,42}.

Utilizing our IRISeq platform, we performed spatial transcriptome analysis on the brains of 23-month-old WT and the two types of aforementioned immunodeficient mice (three replicates per group) (Fig. 6a). We profiled a total of 45 coronal sections—including representative sections from the frontal, middle and dorsal cortex (Fig. 6a and Supplementary Table 2)—thereby covering brain regions from the isocortex to areas such as the hippocampus, thalamus and hypothalamus. After quality-control filtering to remove low-quality receiver beads, we recovered a median of 7,470 beads per section, yielding 363,777 spatially distinct transcriptome profiles (Fig. 6b and Extended Data Fig. 10). Bead-connection data enabled us to reconstruct the spatial distribution of beads across the sections, which mapped them to specific brain regions consistent with their annotations (Fig. 6c).

To study lymphocyte deficiency-driven transcriptome changes, we next performed differential gene expression analysis across 25 brain regions, identifying 597 upregulated genes and 790 downregulated genes (FDR < 0.05 with more than twofold changes between WT and mutant brains) (Fig. 6d and Supplementary Table 5). The *Prkdc* mutant uniquely showed upregulation of senescence pathway genes

(for example, *Cdkn1a*, *Btg2*, *Ccnd1*), which is likely a consequence of impaired DNA repair leading to chronic cellular stress in this specific mutant⁴³. Importantly, both *Rag1* and *Prkdc* mutants exhibited increased expression of ependymal cell markers (*Foxj1*, *Ccdc153*, *Rsph1*) and the choroid plexus marker *Ttr*, particularly in the habenular and third ventricle regions. This suggests that lymphocyte deficiency is linked to the preservation of these cell populations (Fig. 6e and Extended Data Fig. 10e). Additionally, we observed a brain-wide decrease of lymphocyte marker genes such as *Igkc*, a B cell marker, validating the depletion of mature B cells. Other genes we observed significantly depleted were primarily associated with the interferon response pathway (for example, *Ifit3*, *Ifit3b*, *Oasl2*) (Fig. 6e). Notably, although interferon-related gene expression was generally reduced in the aged brains of lymphocyte-deficient mutants, the most pronounced decreases were observed in the lateral ventricular regions and white matter, areas that are key sites of inflammation during brain aging²⁸ (Fig. 6e–g). This finding is consistent with our previous observation that aging-associated interferon signatures peak in the ventricular regions (Fig. 4d), thereby underscoring the role of lymphocytes in driving interferon activation and suggesting that targeted ablation could mitigate age-related ventricular inflammation.

To further elucidate lymphocyte-driven mechanisms in brain aging, we analyzed the transcriptional profiles of single cells isolated from brain sections of aged WT and lymphocyte-deficient mice using the EasySci platform¹⁶. In total, we profiled 36 samples: the three brain regions included in our IRISeq analysis, as well as the midbrain and hindbrain regions omitted from our spatial analysis. Samples were derived from WT mice and two immune-deficient genotypes, with three biological replicates per condition. After sequencing and filtering to remove low-quality cells and doublets, we obtained 783,264 high-quality single-nucleus gene expression profiles (Fig. 7a), with an average of 3,155 unique transcripts per cell (median = 2,122 UMIs; Supplementary Fig. 1a). UMAP visualization and Leiden clustering revealed 42 major cell types (Fig. 7b and Supplementary Fig. 1b), which we annotated using predicted labels from published brain atlas data^{16,44} (Supplementary Figs. 2–5), with their anatomical origins further confirming the annotations (Supplementary Fig. 1b).

We next performed a differential gene expression analysis across 42 brain cell types, identifying 9,860 and 7,836 cell-type-specific DE genes in *Rag1* and *Prkdc* mutants, respectively. Among these, 2,113 DE genes were shared between the two mutants, exhibiting significantly consistent changes (Pearson $r = 0.87$, P value < 2.2×10^{-16} ; Fig. 7c). Gene ontology (GO) analysis revealed that the shared upregulated genes were enriched in neurogenesis and axonogenesis pathways (Fig. 7d), consistent with the regulatory function of inflammatory lymphocytes in suppressing neurogenesis⁴⁵. Notably, key immune-response genes

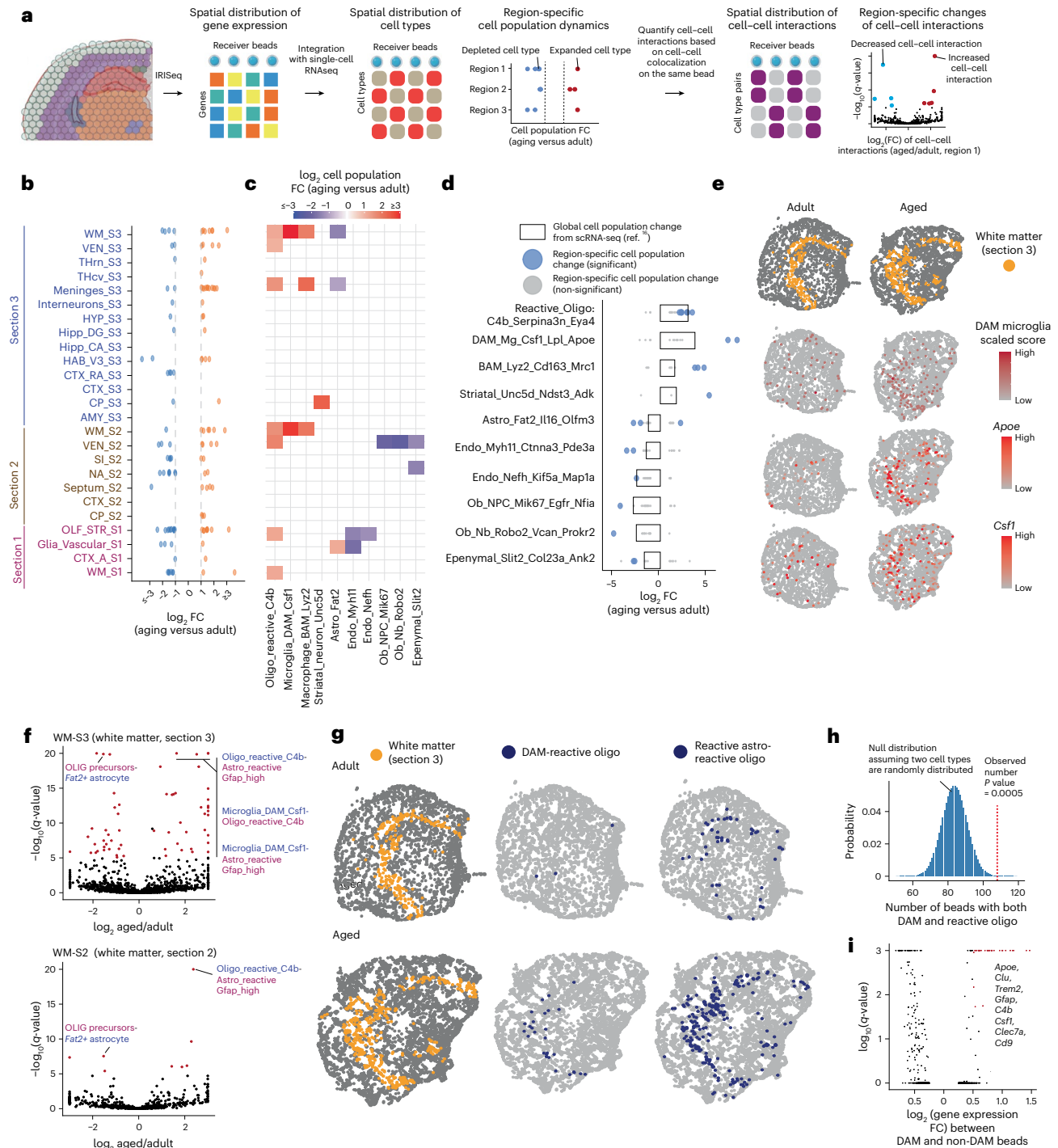
Fig. 5 | Age-associated changes in region-specific cell-type abundance and cell–cell interactions. **a**, Overview of the approach used to identify region-specific cellular depletion or expansion associated with aging and to analyze cell–cell interaction dynamics. **b**, Scatter plot illustrating the number of cell types across different brain regions, showing differential abundance between adult and aged animals. Increases are shown in orange and decreases in blue. Differentially abundant cells were defined by a 1.5-fold change with an FDR < 10^{-5} . **c**, Heatmap showing the FC in key aging-associated cell types across different brain regions. **d**, Both global¹⁶ and region-specific changes (IRISeq) in various cell populations with aging. Significant changes are highlighted to show how specific cell types respond to aging in different brain regions, providing insights into the cellular dynamics associated with the aging process. **e**, Spatial plots depicting DAM microglia and DAM microglia-associated gene localization in the white-matter regions of section 3. **f**, Volcano plot showing significant enrichment and depletion of cell–cell interaction changes in aged versus adult white matter, across two anatomically distinct white-matter regions in sections 2 and 3, highlighting significantly changed cell–cell interactions in aging. **g**, left: representative spatial maps depicting white-matter regions in two

sections from the adult (top) and aged (bottom) brain. Middle: beads indicating colocalization of reactive oligodendrocytes and DAM. Right: beads with both reactive oligodendrocytes and activated astrocytes. **h**, Histogram illustrating the null distribution of beads with both cell types, assuming random distribution, with a dashed line marking the observed number. Colocalization enrichment between cell subtype pairs was assessed by one-sided hypergeometric test within each region after filtering RTCD subtype likelihood values < 0.05; significant interactions were defined by adjusted $P < 0.05$. **i**, Volcano plots comparing gene expression in beads with or without DAM in the white matter of section 3, highlighting the top DEGs. NPC, neuronal progenitor cells; Nb, neuroblasts; scRNA-seq, single cell RNA sequencing. Schematic in a created in BioRender; Cao, J. <https://BioRender.com/i2ew4vq> (2026). Astro, astrocytes; BAM, border-associated macrophages; DAM, disease-associated microglia; Endo, endothelial cells; Ependymal, ependymal cells; Microglia, microglia; Nb, neuroblasts; NPC, neural progenitor cells; Ob_Nb, olfactory bulb neuroblasts; Ob_NPC, olfactory bulb neural progenitor cells; Oligo, oligodendrocytes; Oligo precursor, oligodendrocyte precursor cells; Reactive Astro, reactive astrocytes; Reactive Oligo, reactive oligodendrocyte-lineage cells; Striat, striatal neurons/cells.

(for example, *Igkc*, *Ighm*) were significantly downregulated in both mutants (Fig. 7e). To further validate lymphocyte deficiency in both mutants, we extracted 18,588 immune cells for clustering analysis, which yielded nine distinct immune-cell populations—including T and B lymphocytes as well as different microglia subtypes—based on cell-type-specific markers (Fig. 7f,g and Supplementary Fig. 5). Differential abundance analysis using Milo⁴⁶ confirmed a significant depletion of lymphocytes in the mutants, as expected (Fig. 7h). In contrast, major microglial subtypes such as proliferating microglia and disease-associated microglia (DAM) showed minimal alterations, suggesting that their dynamics are less affected by lymphocyte depletion. Notably, we identified a unique mutant-specific microglial state characterized by the expression of genes involved in cholesterol biosynthesis

(*Dhcr7*) and calcium homeostasis (*Tmtc2*) (Fig. 7h,i). Although this state has not been reported previously, prior studies have shown that *Dhcr7* is expressed in a subset of microglia, with its deficiency driving increased microglial activation and astrocyte reactivity⁴⁷.

Focusing on the effects of lymphocyte depletion on other brain cell populations, particularly in the aging-vulnerable ventricular regions, our spatial analysis revealed decreased inflammation in both of these ventricular regions in immune-deficient brains and elevated expression of choroid plexus epithelial cells and ependymal cells marker genes in the third ventricle region of section 3 (Fig. 6e,f). Both mutants consistently exhibited reduced pallidal-striatal GABAergic-cholinergic neurons and increased numbers of ventricular-specific choroid plexus epithelial and ependymal cells (Fig. 7j and Supplementary Fig. 6a).



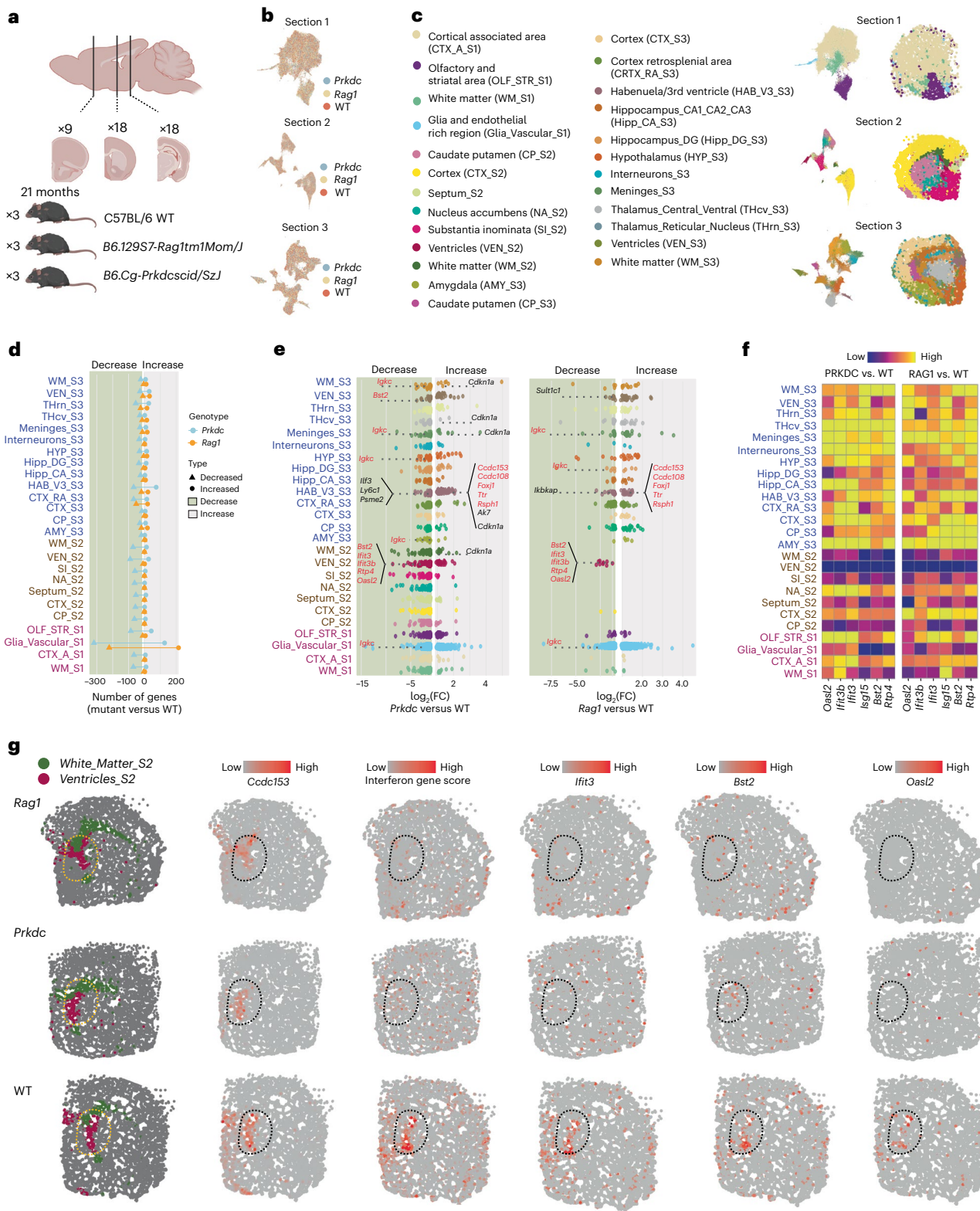


Fig. 6 | IRISeq reveals lymphocyte-dependent shifts in aging-associated interferon gene signatures. a, Schematic of the study design, showing the number of replicates per genotype and anatomical locations in coronal sections. **b**, UMAP visualization of bead-specific gene expression, colored by genotypes. **c**, UMAP visualization of gene expression (left) and spatially reconstructed brain sections (right), colored by annotated brain regions. **d**, Barplot showing the number of DE genes upregulated or downregulated across different identified regions (mutants versus WT). **e**, Dot plot highlighting key upregulated and downregulated genes in immune-deficient mutants. Red-marked genes

indicate DE genes that are shared between both mutants. **f**, Heatmap showing interferon-related gene expression levels in mutants compared to WT (left). **g**, left: highlights the ventricles as anatomical landmarks, with *Ccdc153* gene expression (second from left) marking ventricle ependymal cells. Third from left: aggregated expression of interferon-related genes (*Bst2*, *Ifit3*, *Ifit3b*, *Rtp4*, *Oasl2*) across spatially reconstructed arrays. Fourth–sixth from left: spatial expression of individual interferon-associated genes. Schematic in **a** created in BioRender; Cao, J. <https://BioRender.com/c6n61lz> (2026).

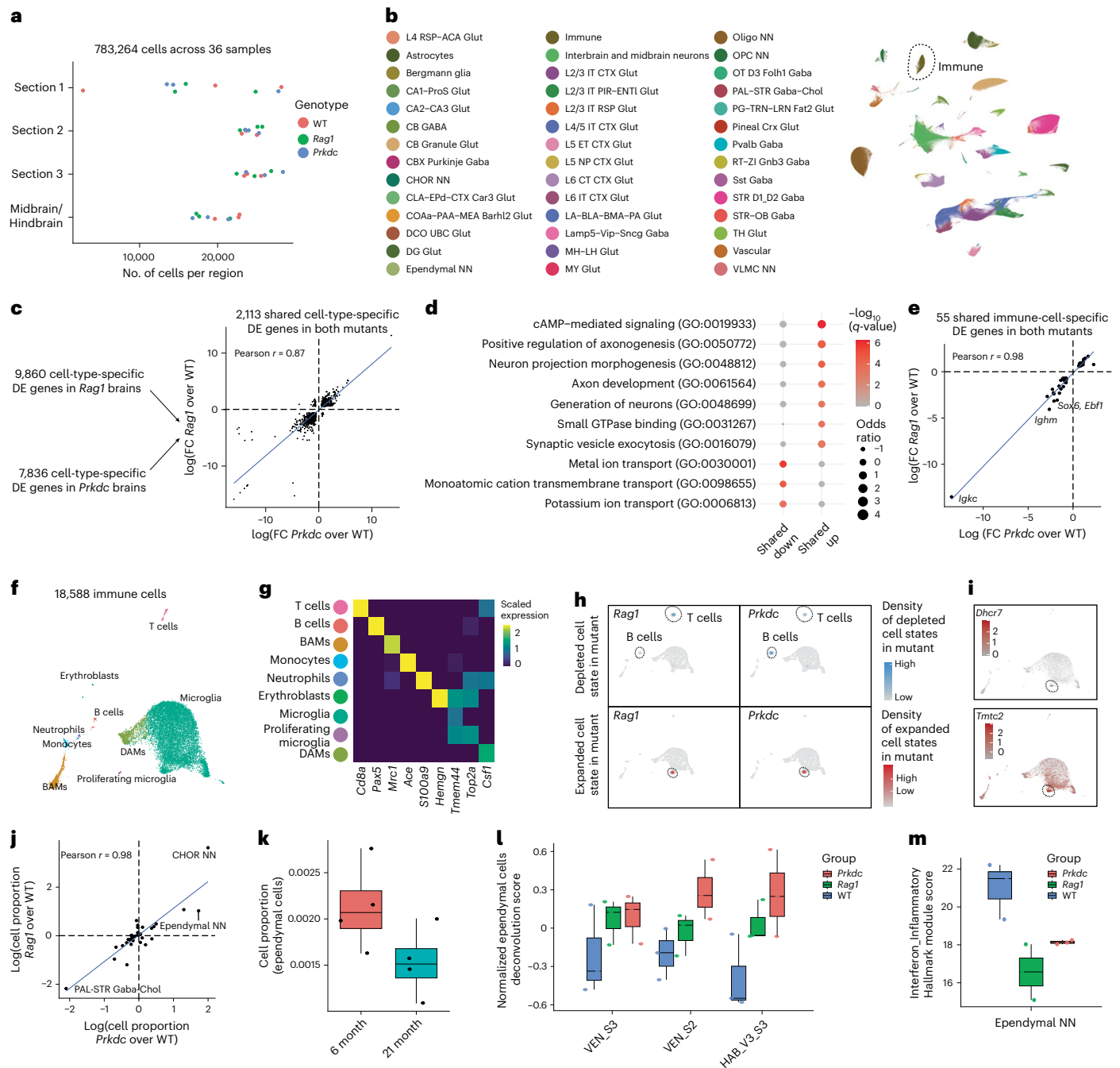


Fig. 7 | Identification of cell-type-specific gene expression and population changes in immune-deficient brains. **a**, Scatter plot of the number of cells profiled per sample across brain regions, colored by genotype. **b**, UMAP projection of all brain cells, colored by annotated major cell types. **c**, DE analysis identifying cell-type-specific DE genes in each mutant compared to WT. The scatter plot demonstrates a strong concordance of DE genes between the two mutants. **d**, Dot plot showing significantly enriched pathways among the upregulated and downregulated DE genes shared by both mutants. **e**, Scatter plot illustrating the high consistency of immune-cell-specific DE genes across both mutants. **f**, UMAP plot of immune cells, colored by annotated immune-cell subtypes. **g**, Heatmap of the relative expression of cell-type-specific marker genes across immune subtypes. Expression is aggregated for each cell type, normalized by library size and log-transformed. **h**, Density plots of mutant-depleted (top) and mutant-enriched (bottom) immune-cell states identified by Milo. **i**, UMAP plot, as in **f**, colored by normalized expression of *Dhcr7* (top) and *Tmtc2* (bottom). **j**, Scatter plot showing the consistent changes in cell populations for both mutants in the hippocampal section (section 3), with top-changed cell types labeled. **k**, Box plot illustrating the decreased proportion of ependymal cells using data from a published brain aging atlas ($n = 4$ biologically independent samples per group). Center line, median; box, interquartile range; whiskers, minimum to maximum. **l**, Barplot showing the normalized deconvoluted proportion of ependymal cells across different brain regions in the IRISeq spatial dataset, with error bars representing standard error. **m**, Box plot showing the aggregated and normalized expression of interferon response genes (Interferon_Inflammatory Hallmark gene set and Supplementary Table 10) across genotypes in ependymal cells from section 3. $n = 3$ biologically independent samples per group for all panels unless otherwise indicated. Center line, median; box, interquartile range; whiskers, minimum to maximum. BAM, border-associated macrophage.

and *Tmtc2* (bottom). **j**, Scatter plot showing the consistent changes in cell populations for both mutants in the hippocampal section (section 3), with top-changed cell types labeled. **k**, Box plot illustrating the decreased proportion of ependymal cells using data from a published brain aging atlas ($n = 4$ biologically independent samples per group). Center line, median; box, interquartile range; whiskers, minimum to maximum. **l**, Barplot showing the normalized deconvoluted proportion of ependymal cells across different brain regions in the IRISeq spatial dataset, with error bars representing standard error. **m**, Box plot showing the aggregated and normalized expression of interferon response genes (Interferon_Inflammatory Hallmark gene set and Supplementary Table 10) across genotypes in ependymal cells from section 3. $n = 3$ biologically independent samples per group for all panels unless otherwise indicated. Center line, median; box, interquartile range; whiskers, minimum to maximum. BAM, border-associated macrophage.

Notably, the elevated abundance of ependymal cells in mutants counteracted their typical age-related decline (Fig. 7k). This observation was further validated by cell-type deconvolution analysis of spatial IRISeq data, which confirmed elevated proportions of ependymal cells in ventricle regions across three different regions (Fig. 7l). We further examined the molecular signatures underlying the increased abundance of ependymal cells in both immune-deficient mutants. Notably, the increased abundance of these cells was accompanied by a marked suppression of interferon signaling (Fig. 7m), which is consistent with our spatial analysis revealing reduced interferon activity in the ventricle region (Fig. 6g). In addition, we identified C3, a critical component of the complement system, to be heavily downregulated in ependymal cells (Supplementary Fig. 6b). Collectively, these findings suggest that immune deficiency creates a molecular environment that favors the preservation of ependymal cells in the aging brain.

Discussion

The limitations of current, often imaging-based, spatial transcriptomics methods^{1–10} in terms of throughput and time led us to develop IRISeq, an optics-free spatial profiling platform using ‘spatial interaction mapping by indexed sequencing’. IRISeq is highly cost-effective (approximately \$30 per tissue section), is scalable for profiling multiple large tissue sections and offers adjustable resolution (5–50 μm bead size). By eliminating the need for imaging or preindexed arrays, IRISeq establishes a versatile and accessible tool for comprehensive spatial transcriptomic analysis across diverse research applications. Our IRISeq analysis of age-related changes across 25 mouse brain regions revealed a downregulation of genes for mitochondrial, ribosomal and neuronal function across almost all brain regions. Conversely, genes related to the complement and interferon pathways, as well as inflammation markers, were predominantly upregulated in specific areas such as the ventricles and white matter, aligning with their increased susceptibility to aging.

Further cell-centric analysis pinpointed precise region-specific changes in cell populations, notably a marked depletion of neurogenesis-related cells in the subventricular zone and the expansion of cell types such as border-associated macrophages and reactive oligodendrocytes. Moreover, our computational pipeline to analyze local cell–cell interactions by assessing the colocalization of two cell types on the same beads revealed a significant, abundance-independent increase in colocalization among disease-associated microglia, reactive oligodendrocytes and activated astrocytes in the aged white matter. This observation aligns with findings from previous imaging-based studies⁴⁸ and validates the effectiveness of our platform in detecting region-specific alterations in cellular networks during aging.

To further investigate the cellular mechanisms underlying region-specific molecular alterations during aging, we applied IRISeq to profile 45 coronal sections from aged WT and two immunodeficient mouse models (*Rag1* and *Prkdc* mutants), yielding 363,777 spatially distinct transcriptome profiles. This analysis revealed both mutant-specific alterations and shared changes that were identified by single-cell analysis of 783,264 high-quality transcriptomes from similar regions. Integrating the spatial and single-cell data validates the key regulatory role of lymphocytes in elevating interferon signaling in ventricular regions and influencing cell population dynamics. Specifically, lymphocyte depletion was associated with the suppression of interferon signaling, the preservation of ependymal cells (counteracting their typical age-related decline) and the emergence of a distinct *Dhcr7*+ *Tmtc2*+ microglial population associated with astrocyte reactivity, whereas canonical microglial populations showed minimal change.

IRISeq is a highly optimized platform for spatial transcriptomics, yet there are opportunities for further improvement. Currently, the method does not provide isolated single-cell information. However, it is readily compatible with nuclei hashing techniques to extend its spatial analysis capabilities⁴⁹. Additionally, IRISeq can be integrated with methods to profile proteins and the epigenetic landscape, broadening

its application spectrum. Further protocol modifications may enable IRISeq to profile formalin-fixed, paraffin-embedded samples. Another limitation is that image reconstruction relies on the stochastic UMAP algorithm¹⁸, which yields digital approximations; however, all critical downstream biological analyses rely on local bead–bead connection information and are unaffected.

In summary, IRISeq demonstrates significant potential for detailed mapping of region-specific molecular signatures, cell population dynamics and local cell–cell interactions across varied and complex biological landscapes. Its capacity to reconstruct images based solely on sequencing local DNA interactions allows for the profiling of tissues without size constraints and across varied resolutions. Looking ahead, the high-throughput, cost-effective nature of IRISeq positions it as a transformative tool for comprehensive spatial mapping of entire organs or organisms, across various genders, ages and disease states. This opens new possibilities for identifying region-specific vulnerabilities linked to different diseases, enhancing our understanding of complex biological systems.

Online content

Any methods, additional references, Nature Portfolio reporting summaries, source data, extended data, supplementary information, acknowledgements, peer review information; details of author contributions and competing interests; and statements of data and code availability are available at <https://doi.org/10.1038/s41593-026-02293-1>.

References

1. Chen, K. H., Boettiger, A. N., Moffitt, J. R., Wang, S. & Zhuang, X. RNA imaging. Spatially resolved, highly multiplexed RNA profiling in single cells. *Science* **348**, aaa6090 (2015).
2. Eng, C.-H. L. et al. Transcriptome-scale super-resolved imaging in tissues by RNA seqFISH. *Nature* **568**, 235–239 (2019).
3. Wang, X. et al. Three-dimensional intact-tissue sequencing of single-cell transcriptional states. *Science* **361**, eaat5691 (2018).
4. Ståhl, P. L. et al. Visualization and analysis of gene expression in tissue sections by spatial transcriptomics. *Science* **353**, 78–82 (2016).
5. Rodriques, S. G. et al. Slide-seq: a scalable technology for measuring genome-wide expression at high spatial resolution. *Science* **363**, 1463–1467 (2019).
6. Liu, Y. et al. High-spatial-resolution multi-omics sequencing via deterministic barcoding in tissue. *Cell* **183**, 1665–1681 (2020).
7. Vickovic, S. et al. High-definition spatial transcriptomics for in situ tissue profiling. *Nat. Methods* **16**, 987–990 (2019).
8. Chen, A. et al. Spatiotemporal transcriptomic atlas of mouse organogenesis using DNA nanoball-patterned arrays. *Cell* **185**, 1777–1792 (2022).
9. Cho, C.-S. et al. Microscopic examination of spatial transcriptome using Seq-Scope. *Cell* **184**, 3559–3572 (2021).
10. Fu, X. et al. Polony gels enable amplifiable DNA stamping and spatial transcriptomics of chronic pain. *Cell* **185**, 4621–4633 (2022).
11. Stickels, R. R. et al. Highly sensitive spatial transcriptomics at near-cellular resolution with Slide-seqV2. *Nat. Biotechnol.* **39**, 313–319 (2021).
12. Boulgakov, A. A., Ellington, A. D. & Marcotte, E. M. Bringing microscopy-by-sequencing into view. *Trends Biotechnol.* **38**, 154–162 (2020).
13. Duan, Z. et al. A three-dimensional model of the yeast genome. *Nature* **465**, 363–367 (2010).
14. Weinstein, J. A., Regev, A. & Zhang, F. DNA microscopy: optics-free spatio-genetic imaging by a stand-alone chemical reaction. *Cell* **178**, 229–241 (2019).
15. Karlsson, F. et al. Molecular pixelation: spatial proteomics of single cells by sequencing. *Nat. Methods* **21**, 1044–1052 (2024).

16. Sziraki, A. et al. A global view of aging and Alzheimer's pathogenesis-associated cell population dynamics and molecular signatures in human and mouse brains. *Nat. Genet.* **55**, 2104–2116 (2023).
17. Delley, C. L. & Abate, A. R. Modular barcode beads for microfluidic single cell genomics. *Sci. Rep.* **11**, 10857 (2021).
18. McInnes, L., Healy, J. & Melville, J. UMAP: Uniform Manifold Approximation and Projection for dimension reduction. Preprint at <https://arxiv.org/abs/1802.03426> (2018).
19. Cao, J. et al. Decoder-seq enhances mRNA capture efficiency in spatial RNA sequencing. *Nat. Biotechnol.* **42**, 1735–1746 (2024).
20. Kleshchevnikov, V. et al. Cell2location maps fine-grained cell types in spatial transcriptomics. *Nat. Biotechnol.* **40**, 661–671 (2022).
21. Bressan, D., Battistoni, G. & Hannon, G. J. The dawn of spatial omics. *Science* **381**, eabq4964 (2023).
22. Langlieb, J. et al. The molecular cytoarchitecture of the adult mouse brain. *Nature* **624**, 333–342 (2023).
23. Ortiz, C. et al. Molecular atlas of the adult mouse brain. *Sci. Adv.* **6**, eabb3446 (2020).
24. Welch, J. D. et al. Single-cell multi-omic integration compares and contrasts features of brain cell identity. *Cell* **177**, 1873–1887 (2019).
25. Cable, D. M. et al. Robust decomposition of cell type mixtures in spatial transcriptomics. *Nat. Biotechnol.* **40**, 517–526 (2022).
26. Miranda-Angulo, A. L., Byerly, M. S., Mesa, J., Wang, H. & Blackshaw, S. Rax regulates hypothalamic tanycyte differentiation and barrier function in mice. *J. Comp. Neurol.* **522**, 876–899 (2014).
27. Campbell, J. N. et al. A molecular census of arcuate hypothalamus and median eminence cell types. *Nat. Neurosci.* **20**, 484–496 (2017).
28. Hahn, O. et al. Atlas of the aging mouse brain reveals white matter as vulnerable foci. *Cell* **186**, 4117–4133 (2023).
29. Gonskikh, Y. & Polacek, N. Alterations of the translation apparatus during aging and stress response. *Mech. Ageing Dev.* **168**, 30–36 (2017).
30. Kumar, V. et al. The regulatory roles of motile cilia in CSF circulation and hydrocephalus. *Fluids Barriers CNS* **18**, 31 (2021).
31. Pastrana, E., Cheng, L.-C. & Doetsch, F. Simultaneous prospective purification of adult subventricular zone neural stem cells and their progeny. *Proc. Natl Acad. Sci. USA* **106**, 6387–6392 (2009).
32. Lim, D. A. & Alvarez-Buylla, A. The adult ventricular-subventricular zone (V-SVZ) and olfactory bulb (OB) neurogenesis. *Cold Spring Harb. Perspect. Biol.* **8**, a018820 (2016).
33. Bennett, H. C. et al. Aging drives cerebrovascular network remodeling and functional changes in the mouse brain. *Nat. Commun.* **15**, 6398 (2024).
34. Ozaki, T. & Sakiyama, S. Molecular cloning and characterization of a cDNA showing negative regulation in v-src-transformed 3Y1 rat fibroblasts. *Proc. Natl Acad. Sci. USA* **90**, 2593–2597 (1993).
35. Zhou, Y. et al. Human and mouse single-nucleus transcriptomics reveal TREM2-dependent and TREM2-independent cellular responses in Alzheimer's disease. *Nat. Med.* **26**, 131–142 (2020).
36. Kenigsbuch, M. et al. A shared disease-associated oligodendrocyte signature among multiple CNS pathologies. *Nat. Neurosci.* **25**, 876–886 (2022).
37. Da Mesquita, S. & Rua, R. Brain border-associated macrophages: common denominators in infection, aging, and Alzheimer's disease? *Trends Immunol.* **45**, 346–357 (2024).
38. Dermitzakis, I. et al. CNS border-associated macrophages: ontogeny and potential implication in disease. *Curr. Issues Mol. Biol.* **45**, 4285–4300 (2023).
39. Dulken, B. W. et al. Single-cell analysis reveals T cell infiltration in old neurogenic niches. *Nature* **571**, 205–210 (2019).
40. Gate, D. et al. CD4 T cells contribute to neurodegeneration in Lewy body dementia. *Science* **374**, 868–874 (2021).
41. Mombaerts, P. et al. RAG-1-deficient mice have no mature B and T lymphocytes. *Cell* **68**, 869–877 (1992).
42. Dorshkind, K. et al. Functional status of cells from lymphoid and myeloid tissues in mice with severe combined immunodeficiency disease. *J. Immunol.* **132**, 1804–1808 (1984).
43. Gurley, K. E., Ashley, A. K., Moser, R. D. & Kemp, C. J. Synergy between Prkdc and Trp53 regulates stem cell proliferation and GI-ARS after irradiation. *Cell Death Differ.* **24**, 1853–1860 (2017).
44. Yao, Z. et al. A high-resolution transcriptomic and spatial atlas of cell types in the whole mouse brain. *Nature* **624**, 317–332 (2023).
45. Wang, T. et al. Activated T-cells inhibit neurogenesis by releasing granzyme B: rescue by Kv1.3 blockers. *J. Neurosci.* **30**, 5020–5027 (2010).
46. Dann, E., Henderson, N. C., Teichmann, S. A., Morgan, M. D. & Marioni, J. C. Differential abundance testing on single-cell data using k-nearest neighbor graphs. *Nat. Biotechnol.* **40**, 245–253 (2021).
47. Freel, B. A., Kelvington, B. A., Sengupta, S., Mukherjee, M. & Francis, K. R. Sterol dysregulation in Smith-Lemli-Opitz syndrome causes astrocyte immune reactivity through microglia crosstalk. *Dis. Model Mech.* **15**, dmm049843 (2022).
48. Allen, W. E., Blosser, T. R., Sullivan, Z. A., Dulac, C. & Zhuang, X. Molecular and spatial signatures of mouse brain aging at single-cell resolution. *Cell* **186**, 194–208 (2023).
49. Srivatsan, S. R. et al. Embryo-scale, single-cell spatial transcriptomics. *Science* **373**, 111–117 (2021).
50. Wang, Q. et al. The Allen mouse brain common coordinate framework: a 3D reference atlas. *Cell* **181**, 936–953 (2020).

Publisher's note Springer Nature remains neutral with regard to jurisdictional claims in published maps and institutional affiliations.

Open Access This article is licensed under a Creative Commons Attribution-NonCommercial-NoDerivatives 4.0 International License, which permits any non-commercial use, sharing, distribution and reproduction in any medium or format, as long as you give appropriate credit to the original author(s) and the source, provide a link to the Creative Commons licence, and indicate if you modified the licensed material. You do not have permission under this licence to share adapted material derived from this article or parts of it. The images or other third party material in this article are included in the article's Creative Commons licence, unless indicated otherwise in a credit line to the material. If material is not included in the article's Creative Commons licence and your intended use is not permitted by statutory regulation or exceeds the permitted use, you will need to obtain permission directly from the copyright holder. To view a copy of this licence, visit <http://creativecommons.org/licenses/by-nc-nd/4.0/>.

© The Author(s) 2026

Methods

Animals

C57BL/6 WT mice, *B6.129S7-Rag1tm1Mom/J* and *B6.Cg-Prkdcscid/SzJ* were acquired from the Jackson Laboratory and the National Institute on Aging colony at Charles River. All mice were housed under standard conditions, with groups matched for sex and age. Mice were socially housed. All animal procedures complied with institutional, state and federal regulations and were approved under IACUC protocols 21049 and 20047. Comprehensive metadata for each animal, including individual ID, sex, age, birth and euthanasia dates, are detailed in Supplementary Table 2. No statistical methods were used to predetermine sample sizes, but our sample sizes are similar to those reported in previous publications. In all studies, we adhere to the recommendations for animal use and welfare, as outlined by Rockefeller University, the Comparative Bioscience Center and the guidelines established by the NIH. The Federal Animal Welfare Assurance number for Rockefeller University is A3081.

IRISeq library preparation

A detailed step-by-step IRISeq protocol is included as a supplementary protocol (Supplementary Note 1).

Brain nuclei extraction for EasySci

The samples were processed by EasySci with minor modifications. In brief, 40- μm -thick, cryosectioned, frozen brain tissues were added to a 6-cm cell culture dish containing 3 ml of lysis buffer solution (EZ Lysis Buffer containing 1% diethylpyrocarbonate). Each sample was homogenized with a razor blade until the solution could be aspirated with 1,000- μl tips to pass through a 40- μm filter above a 50-ml tube that contained 6 ml of lysis buffer solution. We then used the plunger from a 10-ml syringe to further homogenize the tissue on the filter until the solution passed through the filter completely. The filters were washed with 1 ml of additional lysis solution. The nuclei were concentrated by centrifugation at 500g for 5 min at 4 °C. The nuclei were washed three times in nuclei wash buffer (NWB) containing nuclei buffer (10 mM Tris-HCl pH 7.5, 10 mM NaCl, 3 mM MgCl₂ in RNase-free water) supplemented by 1% of 10% Tween-20 diluted in RNase-free water, 1% recombinant albumin (NEB, cat. no. B9200S) and 0.1% SUPERase-In RNase Inhibitor. After the washes, nuclei were aliquoted into two cryovials containing 500 μl of nuclei resuspended in NWB containing 10% dimethyl sulfoxide and stored in slow freezers, cooling at 1 °C per minute, at -80 °C overnight.

The following day, one aliquot of the nuclei from each sample was rapidly thawed in a 37 °C water bath and centrifuged at 500g for 5 min at 4 °C. The supernatant was removed, and the nuclei were resuspended in freshly prepared NWB containing 0.005 mg ml⁻¹ DAPI (Thermo Fisher, cat. no. D1306) for fluorescence-activated cell sorting. The nuclei were stained for 10 min before performing fluorescence-activated cell sorting on a SH800 Cell Sorter with a 100- μm sorting chip (Sony, cat. no. LE-C3210), to capture all DAPI-positive singlet nuclei and to exclude cellular debris and doublet cell populations. Nuclei were collected into a 1.5-ml DNA Lo-Bind tube containing 100 μl of NWB, vortexed to coat the tubes for optimal nuclei capture and subsequently centrifuged at 500g for 5 min at 4 °C before proceeding directly to library construction.

EasySci library construction and sequencing

The subsequent steps for the generation of sequencing libraries followed the published EasySciRNA protocol¹⁶. Initially, the sorted nuclei were distributed across 96-well plates (Geneseesci, cat. no. 24-302) for RT. Before RT, indexed oligo-dT and indexed random hexamer primers were utilized to introduce the first index. The nuclei were pooled, washed and redistributed into new 96-well plates for the addition of the second index through ligation. After subsequent pooling and washing steps, the nuclei were diluted to 500 nuclei μl^{-1} and distributed into new plates for second-strand synthesis and 1 \times AMPure XP SPRI purification

(Beckman Coulter, cat. no. A63882). After elution of the complementary DNA (cDNA), tagmentation with Tn5 transposase was performed, followed by a 16-cycle PCR reaction. The resulting PCR products were then pooled and purified twice using 0.8 \times volume of AMPure XP SPRI. The library concentration and fragment size were measured using an Agilent TapeStation, and sequencing was carried out on an Illumina NovaSeq 6000 System with an S4 Flow Cell.

Computational procedures for processing IRISeq libraries

Bead-connection processing. Following the sequencing process, data from two beads—receiver beads and sender beads—were obtained, with UMIs used to identify and quantify individual connection molecules. Reads were classified into R1 (receiver-bead barcodes) and R2 (sender bead barcodes) and mapped to a whitelist of barcodes with a one base pair error tolerance. Duplicated reads were filtered out based on UMIs, and a comma-separated value file was generated containing the receiver-bead barcode, UMI and sender bead barcode, where each line represented a unique molecular connection between beads.

To ensure data quality, connections between beads with fewer than seven UMIs were filtered out. A matrix was then generated, with each row representing a receiver bead, each column representing a sender bead, and the values corresponding to the number of UMIs for each connection. PCA was applied to this matrix to reduce dimensionality while preserving variance, using an elbow plot to determine the optimal number of principal components, typically capturing around 80% of the variance. Subsequently, UMAP was performed on the PCA matrix to further reduce dimensionality, using parameters such as a minimum distance of -0.2 and approximately -20 neighbors to obtain a square-shaped projection. UMAP coordinates for each receiver bead were saved in comma-separated value files for spatial mapping. For larger arrays, UMAP was run on a GPU with increased training epochs (from -500 to -10,000 or more) to handle the larger data matrix. Additionally, for large-array analysis, density-based spatial clustering of applications with noise was applied post-UMAP to remove several erroneously mapped beads⁵¹. A detailed workflow is summarized in Supplementary Fig. 2.

cDNA data matrix processing

After the sequencing process, the data were obtained as two sets of FASTQ files. The first set of FASTQ files (R1.fastq) contained the barcode sequences for receiver beads along with their associated UMIs, and the second set of FASTQ files (R2.fastq) contained the tagmented cDNA sequences. The barcode sequences from R1.fastq were mapped to a whitelist of bead barcodes with a tolerance of one base pair error, and the identified bead barcode was added as an identifier for the corresponding sequences in R2.fastq. New Read2 files were then generated, incorporating the corresponding Read1 barcodes in the sequence names, and any poly(A) tails present at the end of the sequences were trimmed for accurate mapping and analysis. The filtered and trimmed reads were mapped to the reference genome using STAR (Spliced Transcripts Alignment to a Reference)⁵² to align the sequences from R2 to the genomic sequences, identifying their locations and potential splice sites. Duplicate reads were identified and removed post-mapping to eliminate redundant data and ensure accuracy in downstream analysis, resulting in new sequence alignment map files containing the mapped reads with duplicates removed. Finally, gene count matrices were generated from the processed sequence alignment map files for each receiver bead, quantifying the number of reads aligned to each gene and providing information about gene expression levels.

EasySci sequencing data preprocessing

Binary base call files were demultiplexed using the barcode information from the last round of PCR indexing utilizing Illumina's bclfastq2 program (version 2.20.0.422) to convert the file format to FASTQ.

For single-nucleus RNA-seq, read alignment and gene/exon count matrix generation were conducted using our EasySci pipeline (<https://github.com/JunyueCaoLab/EasySci>). Cells from the gene count matrix were filtered according to the following parameters: unmatched rate less than 0.4, combined shortdT and randomN UMI count less than 200 and gene counts less than 100. Scrublet (version 0.2.3) was utilized for the doublet removal set with the following parameters: `min_count = 3`, `min_cells = 3`, `vscore_percentile = 85`, `n_pc = 30`, `expected_doublet_rate = 0.08`, `sim_doublet_ratio = 2`, `n_neighbors = 30`. Cells with a doublet score of more than 0.2 were discarded, which corresponded to 10% of the processed and filtered dataset.

Dimensionality reduction, clustering and region annotation for IRISeq spatial dataset

Raw data from the cDNA sequencing experiment, presented as receiver bead-by-gene expression matrices, underwent several pre-processing steps. The first step included removing beads with low UMI counts (fewer than 600 for the mouse aging dataset). The second step included dividing the dataset according to the anatomical sections by which tissue sections were cryosectioned. LIGER objects were constructed by first normalizing the number of UMIs²⁴. Then the 2,000 highest variable features were selected for each tissue section, followed by scaling of gene expression features. After data normalization and processing, each anatomical dataset with associated individual tissue sections was integrated by LIGER's non-negative matrix factorization (iNMF) approach, followed by UMAP mapping. Louvain clustering was then performed on the normalized NMF factor loadings. Clusters with low UMI and non-specific gene features were iteratively removed to ensure data quality, followed by using the LIGER iNMF workflow to recluster and run UMAP again until no low-quality clusters were formed.

Brain region identification was performed based on NMF factors, gene markers and performing Wilcoxon differential expression (DE) analysis for each identified cluster. A similar analysis scheme and data processing were performed for IRISeq and 10x Visium integration analysis and 10x Visium aging validation analysis. Similar normalization and scaling were done for IRISeq high-resolution data analysis.

Large-area dataset analysis (Fig. 1) was performed utilizing Scanpy⁵³ for PCA followed by UMAP. Leiden clustering was implemented using Scanpy⁵³ to group beads with similar gene expression profiles. Additionally, beads within each cluster were annotated by utilizing differential gene expression analysis for each cluster and associated cluster-specific genes to known cell type and/or brain regions, along with utilizing genes and/or cluster mapping onto spatial anatomical location.

DE analysis for spatial IRISeq data, and EasySci single-cell RNA sequencing

In our DE gene analysis, we employed the likelihood-ratio test to identify aging DE for specific regions using Monocle2⁵⁴. DE genes were filtered based on the following cutoffs: q -value < 0.05 , with FC > 3 between the maximum and second expressed condition and with transcripts per million (TPM) > 50 in the highest expressed condition. FC > 2 was used for mutant spatial IRISeq data to capture more shared signals, because fewer genes met the stricter cutoff.

Cell-type deconvolution

To perform cell-type deconvolution, we applied RCTD²⁵, a computational method that uses cell-type profiles from single-cell RNA-seq to decompose cell-type mixtures while accounting for differences across sequencing technologies. We integrated IRISeq spatial expression data with a single-cell transcriptome dataset from an earlier study¹⁶ following parameters suited for ~ 50 - μm -sized spots and excluded cell types not present in the microdissected sections. For deconvolution of 10- μm -sized beads, we adjusted the RCTD parameters accordingly

and utilized a previously published study with a single-cell reference derived from a brain region similar to the one we profiled²⁰.

Differential abundance analysis for IRISeq

To perform cell abundance analysis across different regions, first, RTCD maximum-likelihood cell-type proportions were binarized by assigning them to one of five categories: values less than 0.05 were categorized as 0, values between 0.05 and 0.2 as 1, values between 0.2 and 0.6 as 2, values between 0.6 and 0.8 as 3 and values greater than 0.8 as 4. This method allowed for transforming continuous proportion data into discrete categories, facilitating subsequent analysis and visualization. After this, a count matrix of receiver bead by cell subtypes was obtained. We later converted raw counts of cell subtypes into normalized counts per million. For differential abundance analysis of cell subtypes, we used the negative binomial model, a common approach for differential gene expression analysis that is well-suited for count data and large-scale datasets. We used a likelihood-ratio test to identify differentially abundant cell subtypes, employing the differentialGeneTest() function of Monocle2 (version 2.28.0)⁵⁴.

For FC calculations, we first normalized the cell counts for each cell subtype relative to the total cell count in each condition. We then compared these normalized values between case and control conditions, adding a small numerical value (10^{-6}) to reduce noise from very small clusters. To classify a cell subtype as a 'significantly changed cell subtype', we set criteria of a maximum FDR of 1×10^{-5} and FC greater than 2 between conditions. We quantified the abundance of aging-associated cell subtypes in the different annotated brain regions by performing differential abundance tests comparing adult and aged samples. Recognizing that variations in one cell subtype can influence the relative proportions of others, particularly static cell subtypes, our analysis focused on cell subtypes exhibiting significant changes: more than a 2 shift in population during aging. This approach was based on the observation that many significantly changed cell clusters corresponded to rare cell states and represented a small portion of the global cell population. Consequently, even if these changing cell subtypes had a substantial impact on others, we expected the overall relative proportion shifts to remain within a twofold range.

Differential abundance analysis for single-nucleus dataset

To assess cell population dynamics across different conditions, we conducted the differential abundance test as demonstrated in ref. 18. Briefly, cell count matrices across replicates (cell population \times replicates) were constructed by counting the cell numbers of each cell population and then normalized against the total cell number recovered from a specific replicate. We then employed the likelihood-ratio test to identify differentially abundant cell populations using the differentialGeneTest() function of Monocle2 (version 2.28.0). For FC calculations, we first normalized the number of cells in each cell population relative to the total cell count in the respective condition. We then compared these normalized values between the case and control conditions, incorporating a small numerical value (10^{-6}) to reduce the noise from very small clusters. To assess the significance of cell population dynamics of specific cell populations, we used an FDR threshold of 0.05 and FC higher than 2 between conditions.

Cell-cell interaction analysis

To assess whether the increased spatial interaction of specific cell subtypes was due to their expansion, we performed a hypergeometric test. This test compared the observed number of beads with colocalized cell types against a null model that assumed a random distribution of cell subtypes colocalization within the region. Before conducting the hypergeometric test, we created a new receiver bead by cell-cell interaction matrix. We generated this matrix by first filtering out low-RTCD-likelihood probability values (< 0.05) for subtype deconvolutions. Next, we conducted a pairwise analysis of cell subtype

coexistence on the same bead. If two cell subtypes had a positive value after filtering out low-RTCD-likelihood probability values, we added a count of 1 to the corresponding cell–cell interaction column. Using the hypergeometric test, we defined the total number of beads within the region (N), the number of beads with a specific cell subtype-subtype interaction (k), the number of beads where colocalization was observed (n) and the number of beads with the other interacting cell subtype (x). The hypergeometric probability $P(X = x)$ was calculated as

$$P(X = x) = \frac{\binom{k}{x} \binom{N-k}{n-x}}{\binom{N}{n}}$$

This formula determined the likelihood of observing the number of colocalized cell subtypes under the null hypothesis.

Single-cell clustering and annotation analysis

For clustering analysis of the single-cell RNA-seq dataset, we first integrated our data with a published EasySci brain atlas¹⁶. The EasySci atlas, which contains approximately 1.5 million cells, was subsampled to 126,285 cells by selecting 5,000 cells from each major cell population (using all cells for populations with fewer than 5,000 cells). We then integrated this subsampled atlas with our full dataset using the integration function in Seurat^{55,56}. Briefly, each dataset was normalized, and the top 5,000 highly variable features were selected using the ‘vst’ method. Integration features were identified with the `SelectIntegrationFeatures()` function, and integration anchors were determined using `FindIntegrationAnchors()`. The datasets were then merged using the `IntegrateData()` function, and clustering was performed with the `FindClusters()` function. To visualize the combined data, all cells were coembedded in a single low-dimensional space.

For cell annotation, we initially employed a support vector machine classifier. Specifically, we used the `LinearSVC` function from `scikit-learn` to train a model on the log-transformed expression values of the subsampled atlas cells, with their corresponding major cell populations as the target variable. The performance of the trained support vector machine was evaluated against a model trained on permuted data before applying it to our full dataset for main cell population prediction. In parallel, we used the BICCN MapMyCells program⁴⁴ (<https://knowledge.brain-map.org/mapmycells/process/>) for hierarchical mapping, retaining high-probability labels for further annotation. Finally, we manually refined the cluster annotations based on the majority vote from the Allen brain atlas⁴⁴ or the EasySci atlas¹⁶ label transfer.

To analyze microglia specifically, we first extracted immune cells from the overall dataset using Seurat⁵⁶ and focused on the top 3,000 highly variable genes. We performed UMAP visualization using the top 30 principal components and set `min.dist = 0.01`. Major immune-cell types were manually annotated based on established marker genes. To identify cellular neighborhoods associated with genotype differences, we applied Milo⁴⁶ using the UMAP coordinates as input, with the following parameters: neighborhood size (k) of 30, dimensionality (d) set to 2 and ‘UMAP’ used for `reduced_dims`. Differential abundance analysis integrated within Milo⁴⁶ was then used to detect cellular neighborhoods that significantly differed between WT and mutant mice (FDR of 0.05).

Differential gene expression analysis with single-cell RNA-seq data

For each major cell population, DEGs between WT and mutant mice were identified using a likelihood-ratio test implemented in Monocle2⁵⁴ (version 2.28.0) via the `differentialGeneTest()` function. We applied stringent criteria to ensure both statistical significance and biological relevance: (1) an FDR threshold of 0.05, (2) an enrichment FC greater than 1.5 when comparing the most highly expressed cell cluster to the

second highest and (3) a maximum TPM value exceeding 50 under specific conditions. The top enriched molecular pathways were identified using gene module enrichment analysis through EnrichR⁵⁷.

Sample size and data exclusion statement. No statistical methods were used to predetermine sample size. The assumptions underlying each statistical test were evaluated before analysis. For parametric tests, normality and equality of variance were assessed where applicable; when these assumptions were not met, nonparametric or distribution-free tests were used. No animals or data points were excluded for downstream analyses.

Reporting summary

Further information on research design is available in the Nature Portfolio Reporting Summary linked to this article.

Data availability

Raw FASTQ files, processed count matrices, cell metadata and gene metadata can be downloaded from NCBI GEO under accession number [GSE270383](https://www.ncbi.nlm.nih.gov/geo/query/acc.cgi?acc=GSE270383).

Code availability

A GitHub repository for data analysis, image reconstruction pipeline, analysis and figures is available at <https://github.com/AbdulAbdulRU/IRISeq>.

References

- Bushra, A. A., Kim, D., Kan, Y. & Yi, G. AutoSCAN: automatic detection of DBSCAN parameters and efficient clustering of data in overlapping density regions. *PeerJ Comput. Sci.* **10**, e1921 (2024).
- Dobin, A. et al. STAR: ultrafast universal RNA-seq aligner. *Bioinformatics* **29**, 15–21 (2013).
- Wolf, F. A., Angerer, P. & Theis, F. J. SCANPY: large-scale single-cell gene expression data analysis. *Genome Biol.* **19**, 15 (2018).
- Qiu, X. et al. Reversed graph embedding resolves complex single-cell trajectories. *Nat. Methods* **14**, 979–982 (2017).
- Stuart, T. et al. Comprehensive integration of single-cell data. *Cell* **177**, 1888–1902 (2019).
- Hao, Y. et al. Integrated analysis of multimodal single-cell data. *Cell* **184**, 3573–3587 (2021).
- Kuleshov, M. V. et al. Enrichr: a comprehensive gene set enrichment analysis web server 2016 update. *Nucleic Acids Res.* **44**, W90–W97 (2016).

Acknowledgements

We thank members of the Cao lab and the Center for Integrated Cellular Analysis (CEGS) for helpful discussions and feedback. We also acknowledge support from Rockefeller University facilities, specifically the Comparative Bioscience Center and High-Performance Computing Center. This work was funded by grants from the NIH (grant nos. 1DP2HG012522, 1R01AG076932 and RM1HG011014 to J.C.) and the Kellen Women’s Entrepreneurship Fund (W.Z.). A.A., T.M., A.D. and A.L. were supported by a Medical Scientist Training Program grant (NIH grant no. T32GM152349). The funders had no role in study design, data collection and analysis, decision to publish or preparation of the manuscript.

Author contributions

J.C. and W.Z. conceptualized and supervised the project. A.A. designed the molecular biology and performed computational analyses (with J.C. and W.Z.); A.A. and W.J. optimized the experimental pipeline with input from Z.X. and T.R., and W.J. processed the IRISeq samples (with A.A.). Z.Z. performed single-cell RNA sequencing

(with A.A.); A.L. and A.D. assisted with other organ experiments. S.I. and A.A. developed the website; T.M. and Z.L. provided insight for data interpretation. W.Z., J.C. and A.A. wrote the manuscript with input and biological insight from all coauthors.

Competing interests

J.C., W.Z., A.A. and W.J. are inventors on pending patent applications related to IRISeg. The other authors declare no competing interests.

Additional information

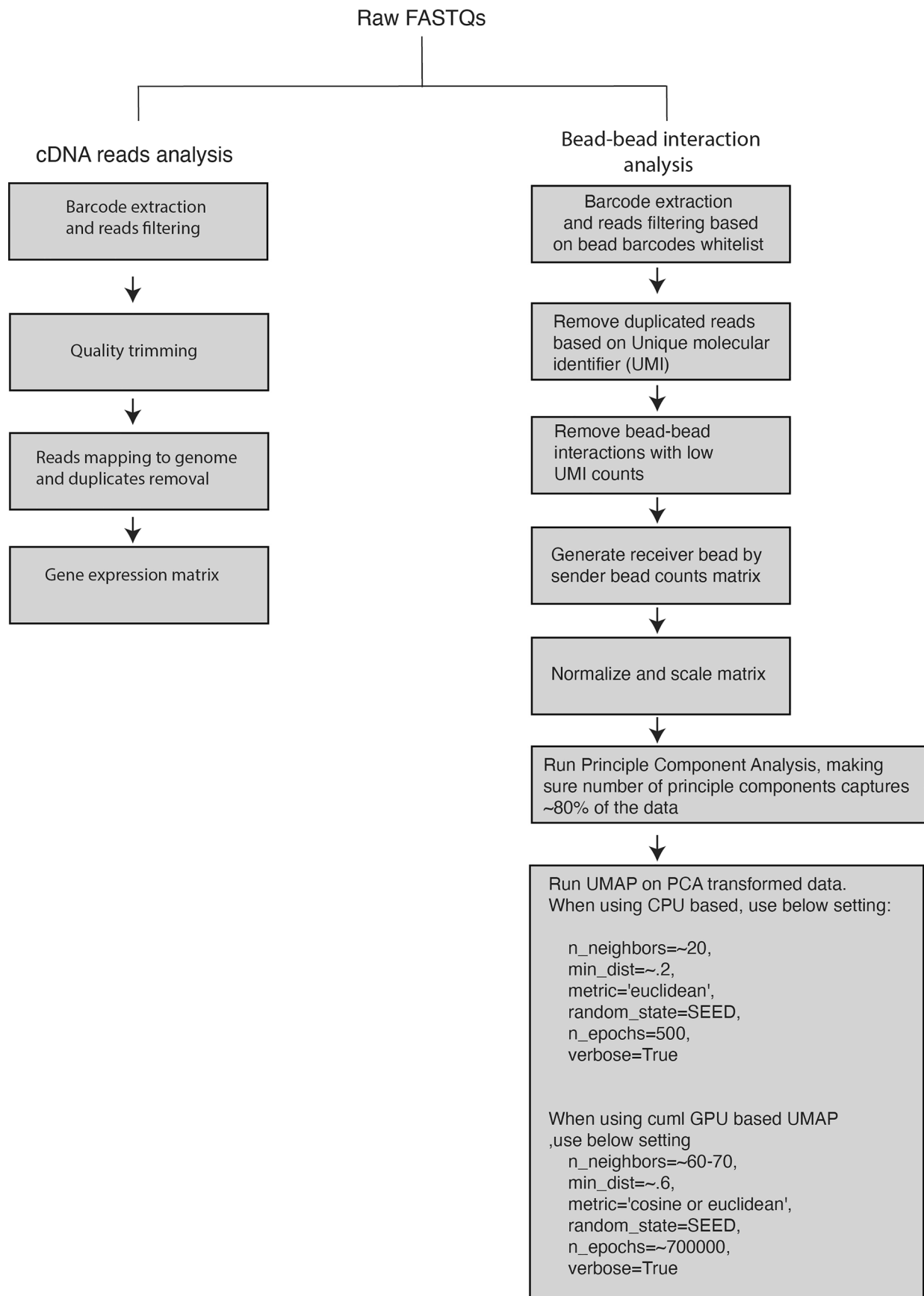
Extended data is available for this paper at <https://doi.org/10.1038/s41593-026-02293-1>.

Supplementary information The online version contains supplementary material available at <https://doi.org/10.1038/s41593-026-02293-1>.

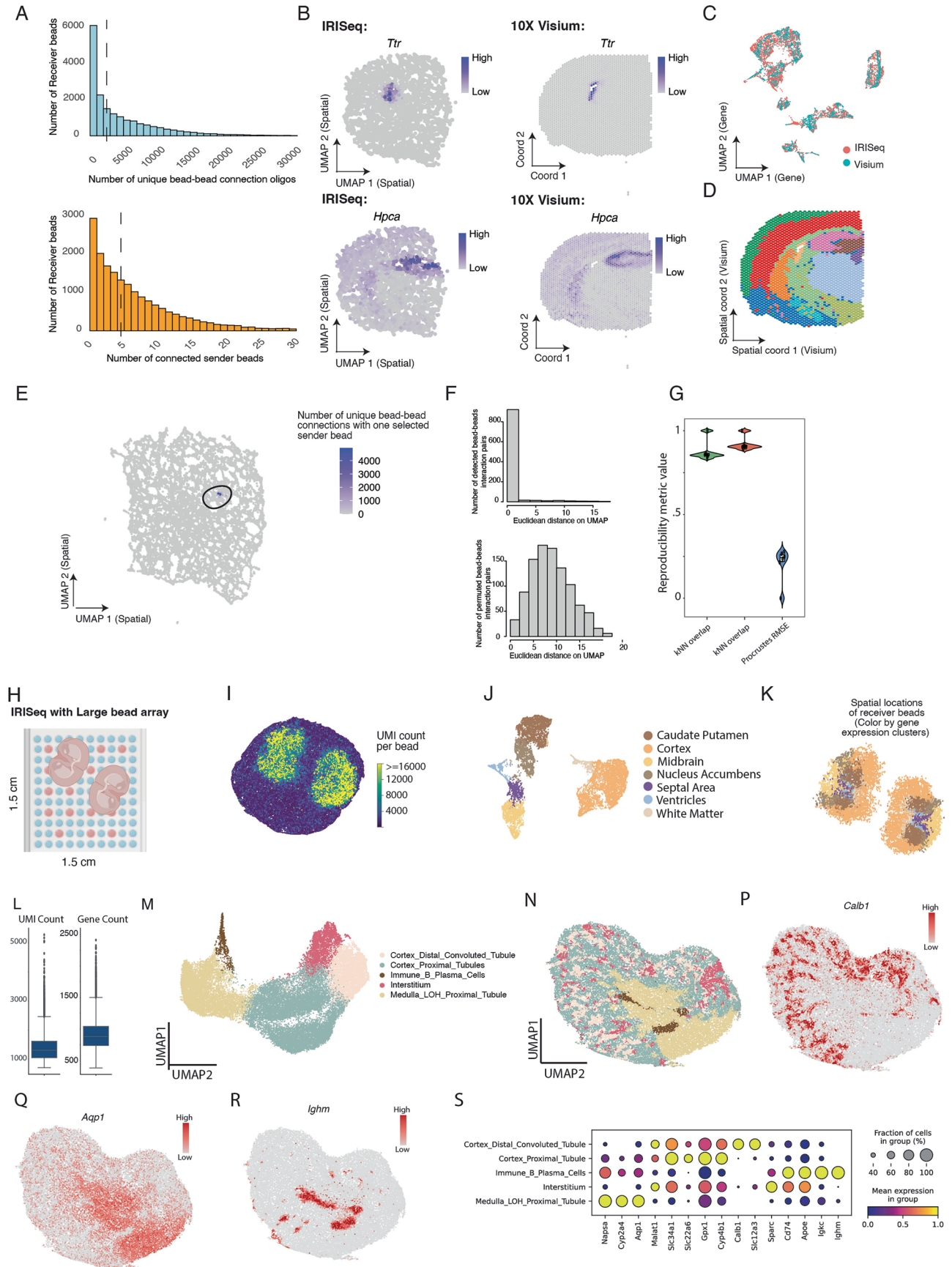
Correspondence and requests for materials should be addressed to Wei Zhou or Junyue Cao.

Peer review information *Nature Neuroscience* thanks Rong Fan and the other, anonymous, reviewer(s) for their contribution to the peer review of this work.

Reprints and permissions information is available at www.nature.com/reprints.



Extended Data Fig. 1 | IRISeq computational pipeline. Customized computational pipeline outlining the derivation of two matrices from each *IRISeq* experiment. The gene count matrix captures gene expression for each bead, while the bead-bead connection counts matrix infers bead locations for image reconstruction.

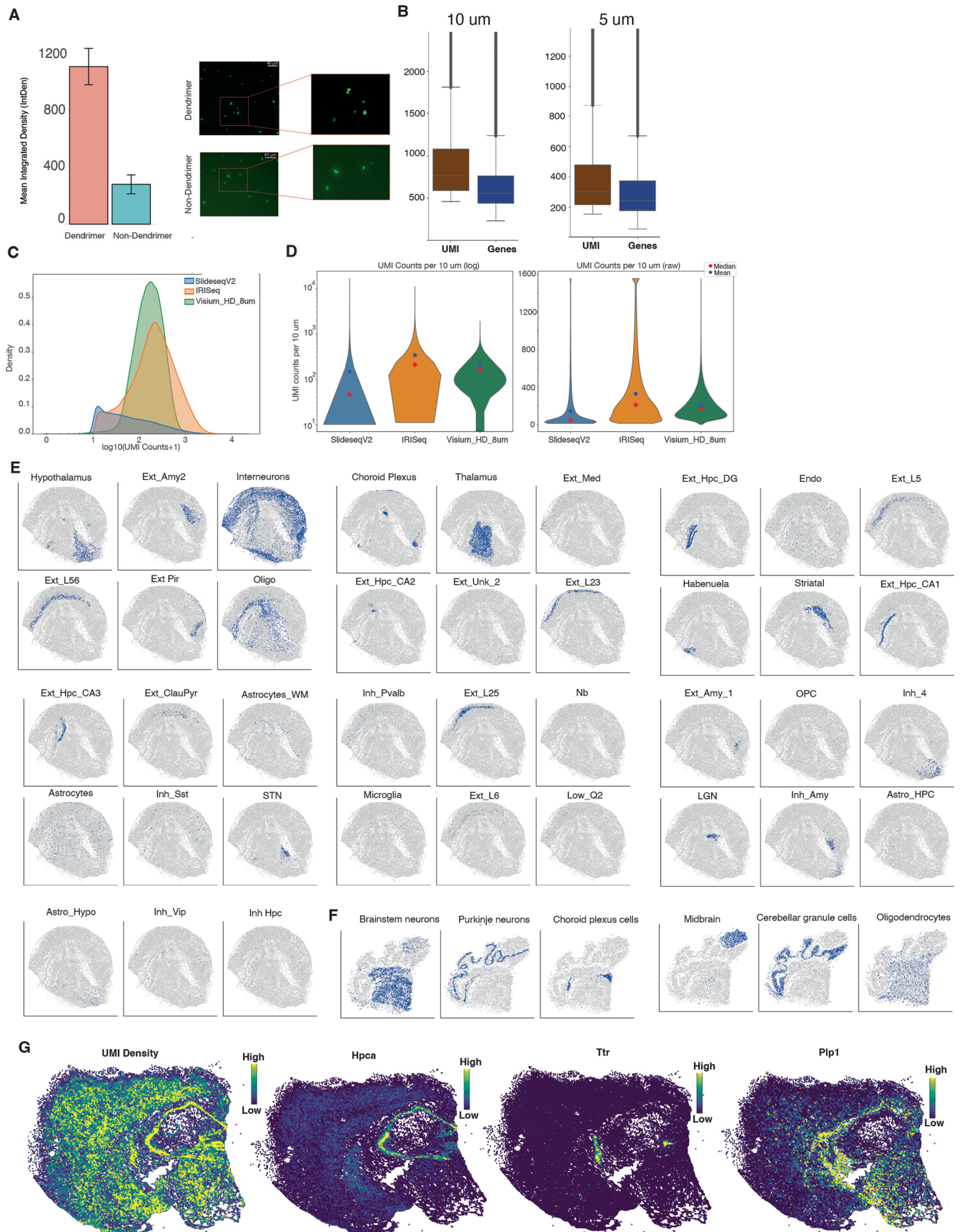


Extended Data Fig. 2 | See next page for caption.

Extended Data Fig. 2 | IRISeq quality control and performance comparison.

(a) The top panel displays the distribution of unique bead-bead interactions per receiver bead. The bottom panel shows the distribution of connected sender beads per receiver bead, with the median indicated by a dashed line in both panels. (b) UMAP plots compare the spatial distribution of receiver beads from a small-scale *IRISeq* experiment (left) with *10x Visium* data (right), colored by the expression of region-specific markers *Ttr* (ventricle region, top) and *Hpca* (hippocampus region, bottom). (c) UMAP plot showing the integrated gene expression profiles from *IRISeq* receiver beads and *10x Visium* spots, colored by assay type. (d) UMAP plot illustrating spatial distribution colored by annotated brain regions, similar to Fig. 1g. (e) UMAP plot showing the reconstructed spatial distribution of receiver beads from *IRISeq*, with beads colored according to the number of unique interaction oligos with a selected sender bead, validating the spatial reconstruction pipeline. (f) Histograms depicting *Euclidean* distances (in Supplementary Fig. 3e) between pairs of receiver beads connected to the same sender bead (top) versus distances between randomly selected receiver beads (bottom). (g) Running UMAP across multiple seeds. UMAP reproducibility

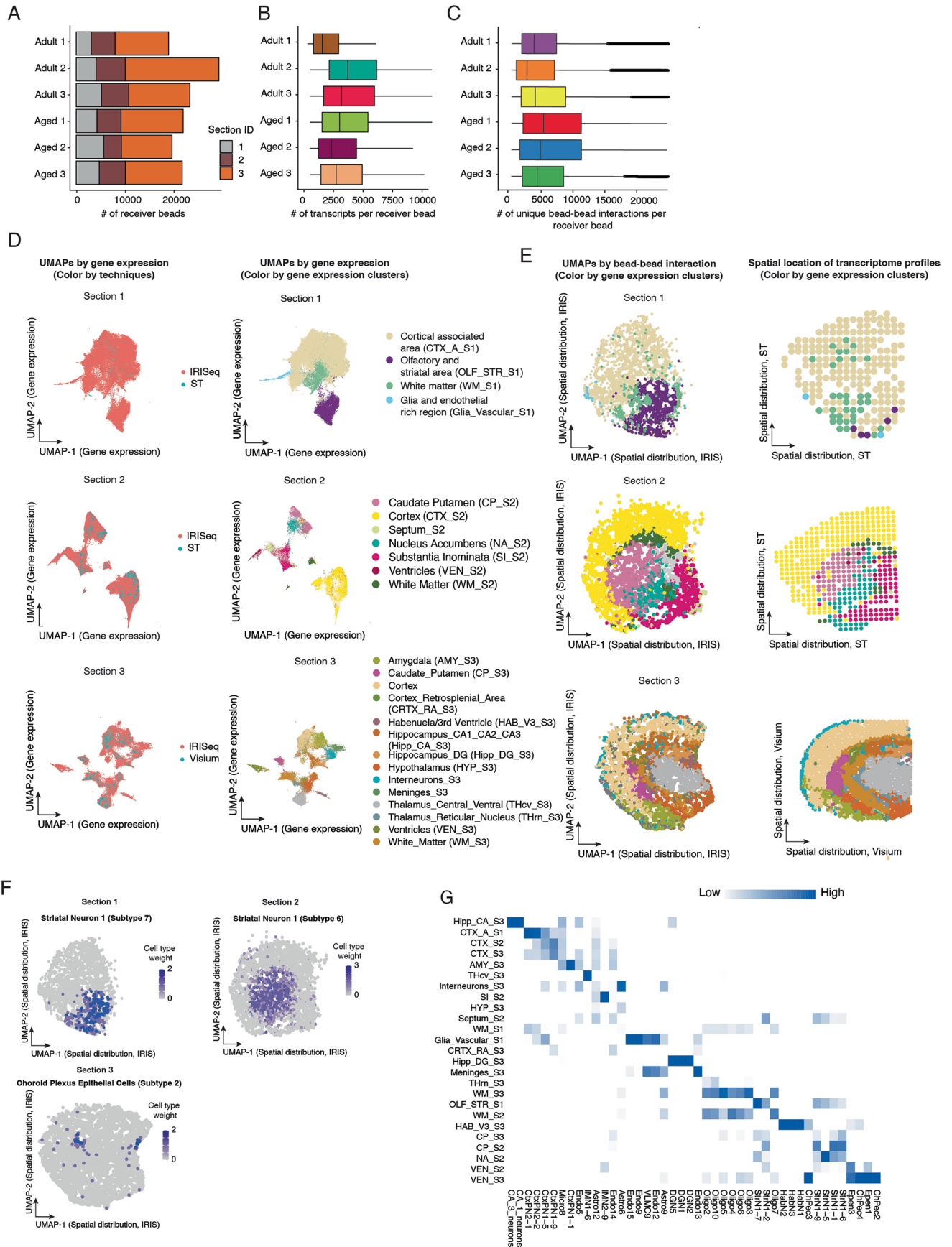
across different seeds. Violin plots show reproducibility metrics across six UMAP runs. Procrustes RMSE (blue) measures global alignment error after orthogonal Procrustes adjustment, while kNN overlap (green = k15, red = k30) reflects local neighborhood stability. (h) Depiction of a large-area *IRISeq* experiment using a 1.5 cm x 1.5 cm bead array to profile two entire brain sections. (i) UMAP plot of receiver beads from the large-area *IRISeq* experiment, colored by the number of unique transcripts detected per bead. (j-k) UMAP plots displaying gene expression clusters (j) and reconstructed spatial distributions (k) of receiver beads from the large-area experiment, colored by annotated brain regions. (l) Quality-control metrics showing the distribution of total UMI counts (left) and detected gene counts (right) per 30 μ m bin following filtering to retain bins with ≥ 700 UMI counts. (m) UMAP visualization of kidney gene expression transcriptomes colored by regional type. (n) Spatial reconstruction of the same dataset showing the spatially resolved distribution of identified regions. (p-r) Spatial plots of gene expression identified to be regionally specific. (s) Dot plot showing regional specific gene expression markers. Schematic in h created in BioRender; Cao, J. <https://biorender.com/i2ew4vq> (2026).



Extended Data Fig. 3 | See next page for caption.

Extended Data Fig. 3 | IRISeq enables spatial transcriptomic profilings at high resolution. (a) Comparison of fluorescence intensities of DNA probes on 5 μm dendrimer-coated beads versus 5 μm non-coated beads. (b) Box plots displaying the distribution of unique transcripts and genes detected per receiver bead in two separate experiments with 10 μm beads (left) and 5 μm beads (right). (c) Kernel density estimation (KDE) plots of \log_{10} -transformed UMI counts, showing the distributional shift across platforms. (d) Left: Violin plots showing per-unit UMI distributions for Slide-seq (10 μm beads), IRISeq (10 μm beads),

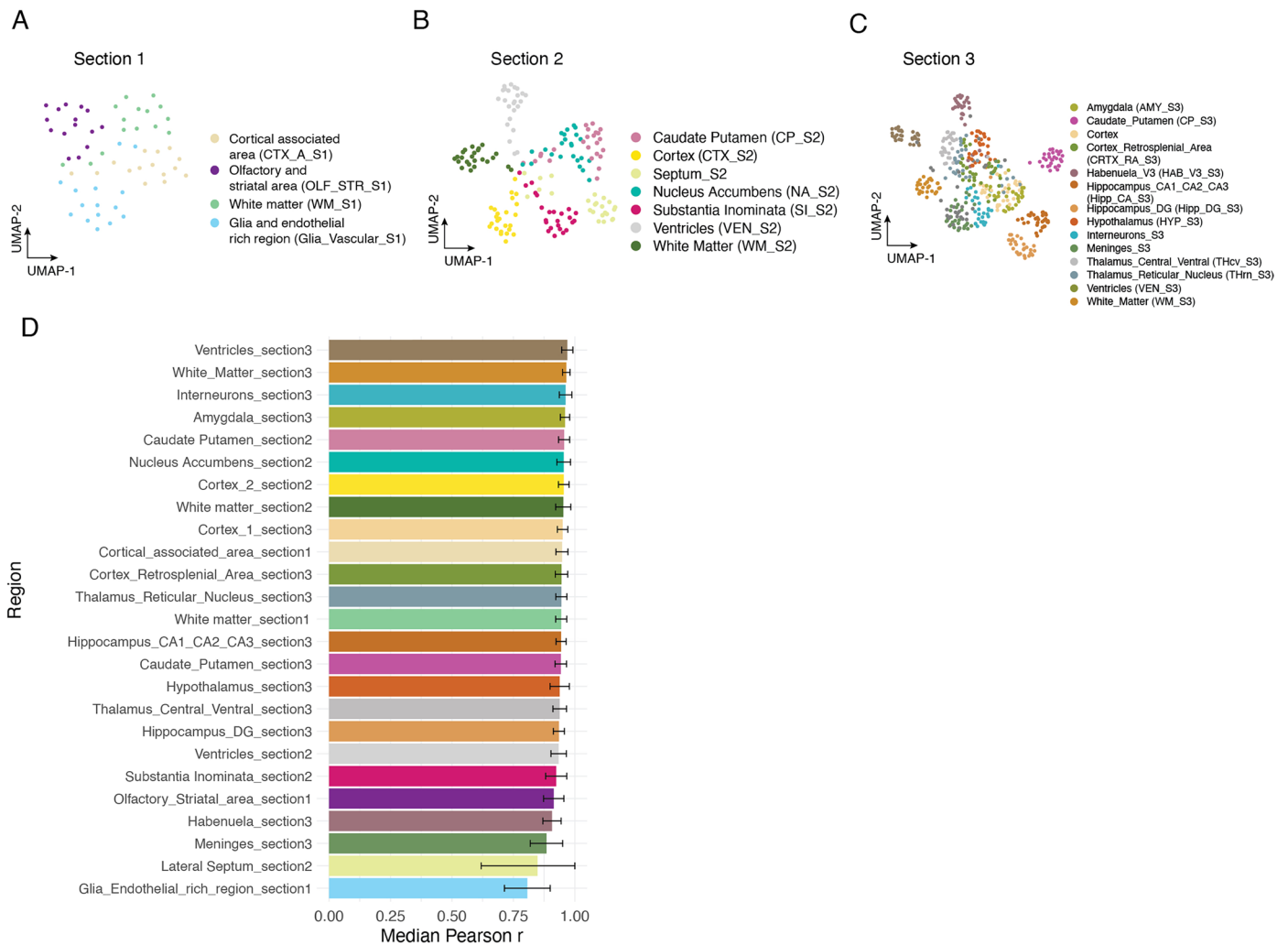
and Visium HD (8 μm bins) on a log scale. Red diamonds indicate median values, and blue circles indicate mean values. Right: Violin plots of the same data clipped at the 99th percentile to highlight differences in the main distribution. Median (red diamond) and mean (blue circle) are shown. (e-f) UMAP plots showing the spatial distribution of 10 μm receiver beads in *IRISeq* experiment described in Fig. 2e,f, colored by cell type annotated clusters; (g) UMI density and detected gene features visualized on the reconstructed 5 μm bead array.



Extended Data Fig. 4 | See next page for caption.

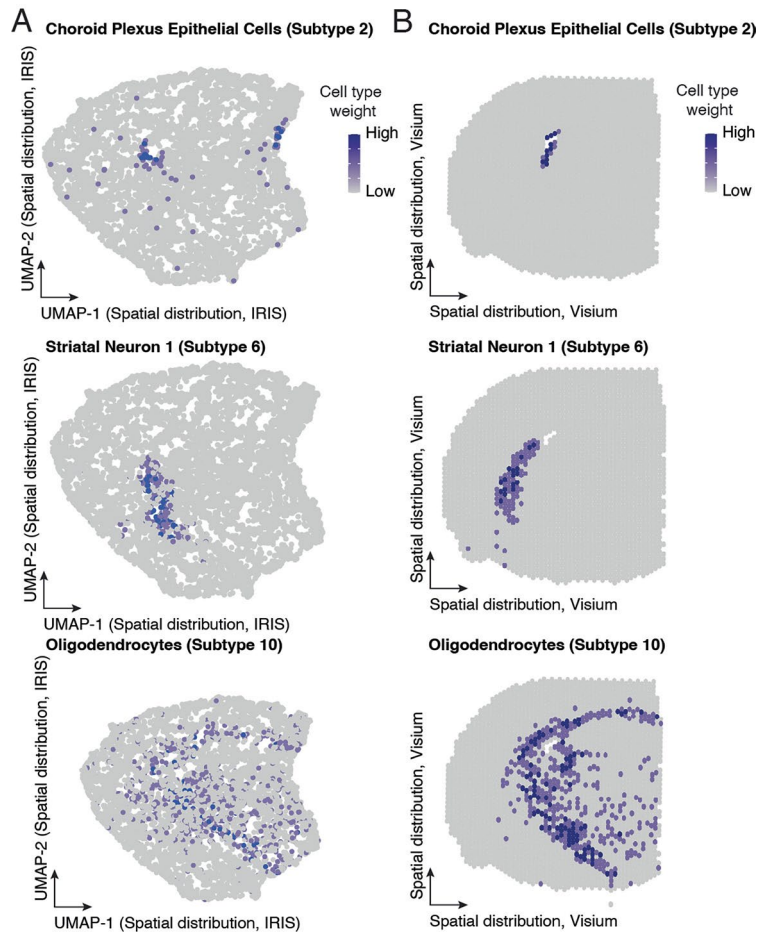
Extended Data Fig. 4 | IRISeq region annotation and published datasets comparison. (a) Barplot showing the number of spatially barcoded receiver beads recovered per mouse individual. (b-c) Boxplots showing the number of unique transcripts (b) and unique bead-bead interactions (c) detected per receiver bead, aggregated across all brain sections for each mouse individual. (d) UMAPs by gene expression comparing *IRISeq* data with published spatial transcriptomics datasets²⁸. The left panels show the gene expression profiles colored by techniques (*IRISeq*, *ST* for spatial transcriptomics, *Visium* for 10X *Visium*), while the right panels color the beads by gene expression clusters specific to each brain region. (e) The left panels depict UMAPs showing the reconstructed spatial distribution of receiver beads from *IRISeq*, colored by gene expression clusters. The right panels display the spatial distribution of transcriptome profiles from published datasets^{18,28} (*ST* for spatial

transcriptomics, *Visium* for 10X *Visium*), with coloring corresponding to the annotated brain regions as identified in the gene expression clustering in (d). (f) cell type weight mapped onto reconstructed tissue representing cell type abundance by *RTCD* analysis²⁹. (g) Heatmap of cell type distribution across regions, showing sub-cluster IDs from the previous single-cell study¹⁸. Cell type weight is calculated using *RCTD*²⁹, integrating published single-cell data¹⁸ with *IRISeq* data, and then regional subtype proportions are aggregated, normalized, and scaled. Cell type abbreviations: DGN: Dentate Gyrus Neurons. CtxPNI: Cortical Projection Neurons I. Endo: Endothelial Cells. Astro: Astrocytes. IMN: Interbrain and Midbrain Neurons. VLMC: Vascular Leptomeningeal Cells. Oligo: Oligodendrocytes. OBN: Olfactory Bulb Neurons. StrN: Striatal Neurons. HabN: Habenula Neurons. Epen: Ependymal Cells. ChPec: Choroid Plexus Epithelial Cells. Micro: Microglia.



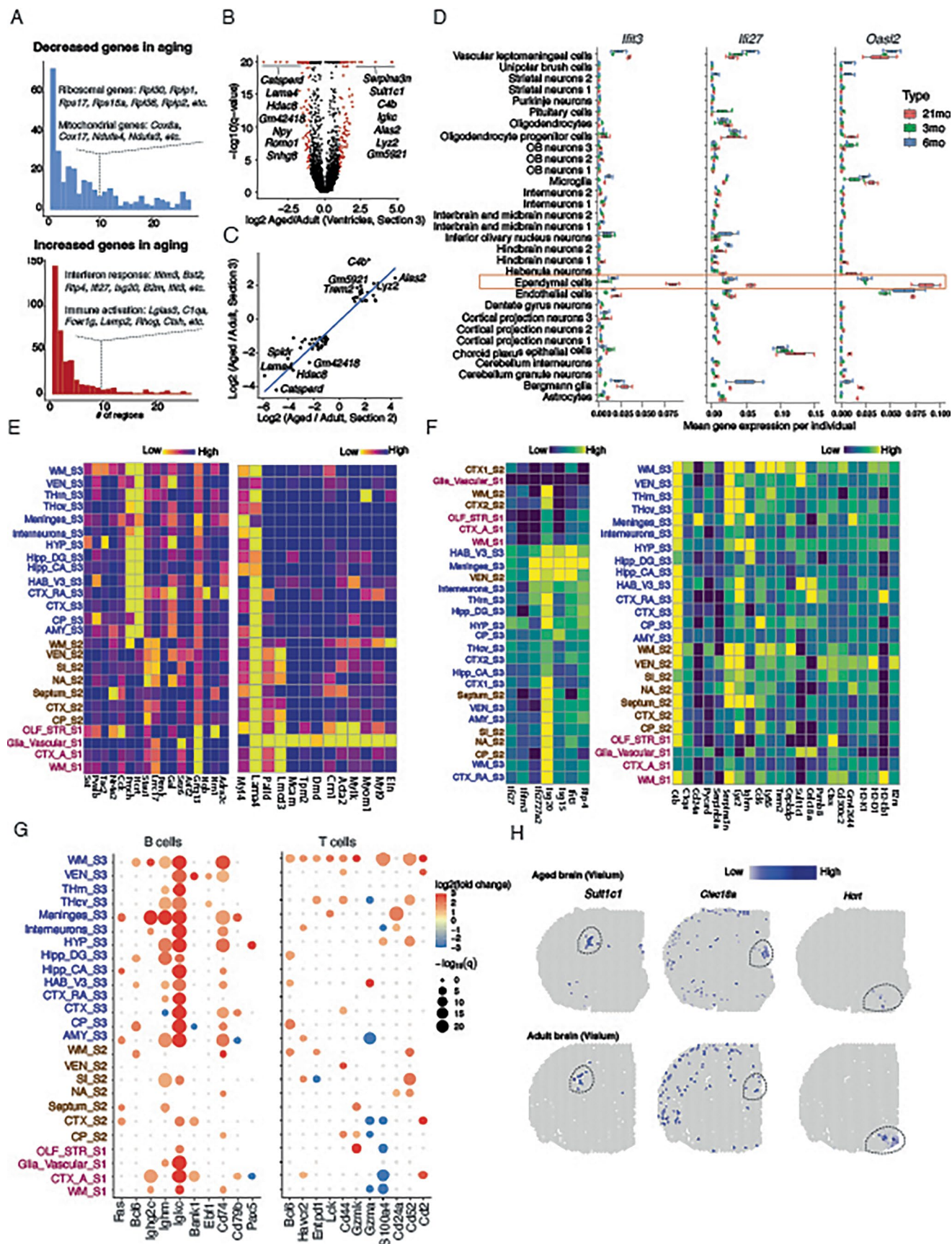
Extended Data Fig. 5 | Cross-replicate consistency of spatial transcriptomic profiles across tissue sections. (a-c) UMAP projections of aggregated, normalized gene expression profiles from each anatomical region in each replicate, from each tissue section, showing that the same regions from different replicates cluster closely together. Each point represents one replicate–region aggregate, colored by anatomical identity. Distinct separation between regions with minimal mixing across replicates demonstrates low replicate-specific

variation relative to biological differences. (d) Ranked barplot showing median pairwise Pearson correlation coefficients between aggregated profiles from the same anatomical region across replicates. Bars are colored by anatomical identity, and error bars represent the interquartile range (IQR). Median correlations range from 0.81 to 0.97, with the majority of regions exceeding 0.93, indicating high reproducibility of spatial transcriptomic profiles despite random bead layouts.



Extended Data Fig. 6 | Comparison of cell subtype distributions between *IRISeq* and *10X Visium*. (a) UMAP plots showing the reconstructed spatial distribution of receiver beads from *IRISeq*, colored by cell type weight. Each plot highlights specific cell types, including Choroid Plexus Epithelial Cells (Subtype 2), Striatal Neuron 1 (Subtype 6), and Oligodendrocytes (Subtype 10), indicating

the abundance of these cell types as determined by RTCD analysis²⁹. (b) Corresponding UMAP plots showing the spatial distribution of transcriptomes generated using *10X Visium*¹⁸, also colored by cell type weight for the same cell types as in panel (a).

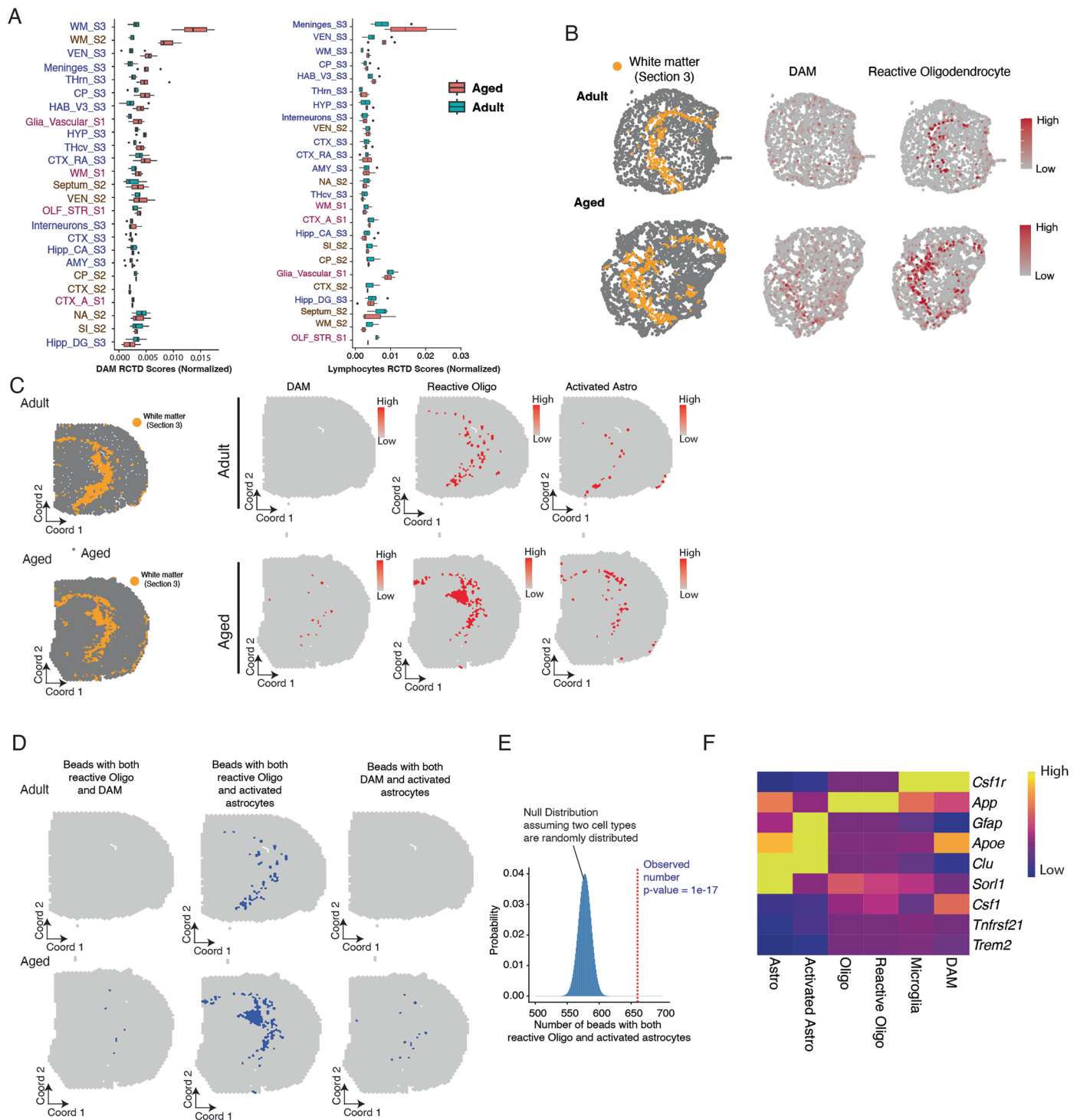


Extended Data Fig. 7 | See next page for caption.

Extended Data Fig. 7 | Region-specific gene expression changes in aging.

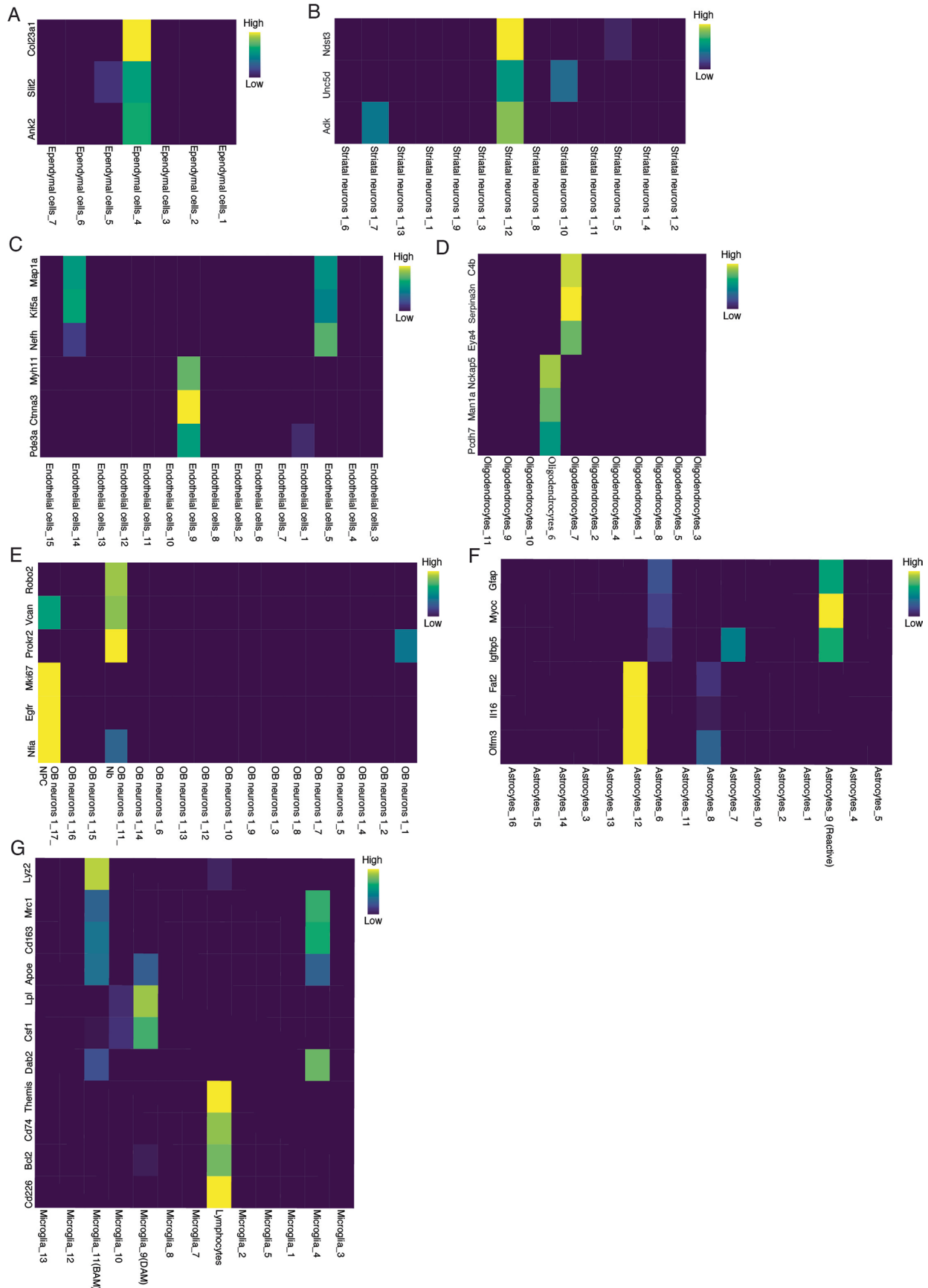
(a) Barplot displays the distribution of down-regulated (top) and up-regulated (bottom) DE genes across regions, highlighting genes consistently altered in more than ten brain regions, grouped by pathway. (b) Volcano Plot showing differentially expressed genes in the ventricles of Section 3 when comparing aged versus adult samples, with significant changes highlighted in red. (c) Scatter plots comparing the alterations in differentially expressed genes between ventricle regions from Sections 2 and 3, including a linear regression line. Only DE genes that are identified in both sections are shown. (d) Cell type-specific expression of interferon-related genes during aging. Aggregated, normalized counts per replicate reveal enrichment of interferon pathway genes in ependymal cells. (e) Representative heatmaps of neuronal-related downregulated genes (left) and downregulated genes involved in smooth muscles (right). (f) Representative heatmaps of interferon related (left) and general inflammatory

marker genes (Right). (g) Dot plot showing significantly upregulated or downregulated lymphocyte-associated transcripts across annotated brain regions. Only genes meeting significance thresholds (false discovery rate [FDR] ≤ 0.05 and raw fold change ≥ 3) are displayed. Dot size reflects the statistical significance ($-\log_{10}[\text{FDR}]$), and color indicates the direction and magnitude of expression change (\log_2 fold change), with red indicating upregulation and blue indicating downregulation. Regions are organized by anatomical grouping, and only significant associations are plotted. (h) Representative aging-associated genes displaying similar upregulation or downregulation patterns in the 10X Visium adult and aging dataset. Center line, median; box, interquartile range; whiskers, minimum to maximum. In panel D, $n = 4$ biologically independent samples per group for all plots unless otherwise indicated. Center line, median; box, interquartile range; whiskers, minimum to maximum.

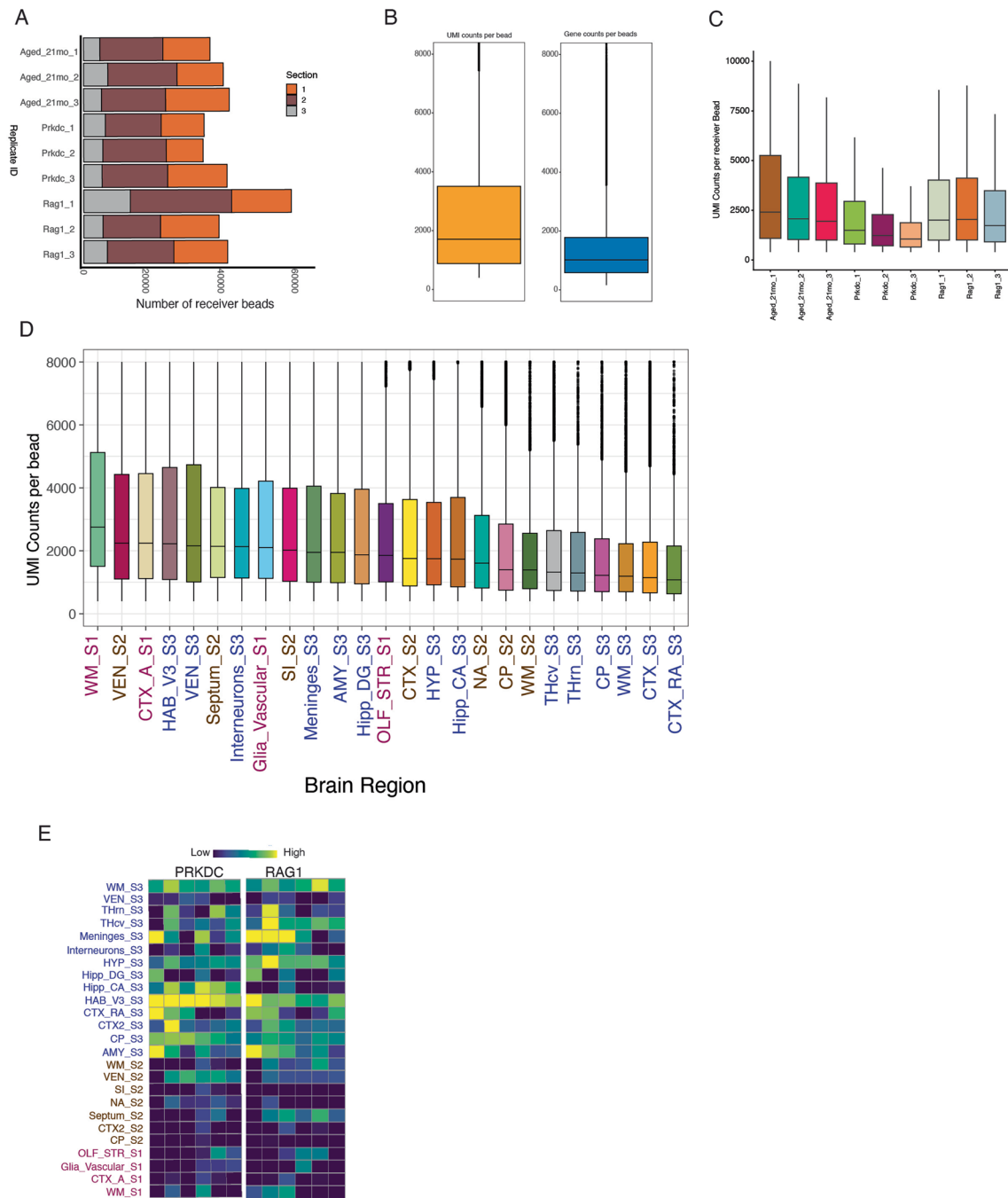


Extended Data Fig. 8 | Region-specific alterations of cellular abundance in brain aging. (a) Box and whisker plot showing RCTD output probability score (Normalized across capture beads per regions) for DAM microglia and Lymphocytes (Non-binarized) across different regions per replicate tissue sections. (b) RCTD probability score for DAM microglia and reactive oligodendrocytes (Non-binarized) across two section-3 adult and aging reconstructed spatial sections. (c) Display of the distribution of DAM, reactive oligodendrocytes, and activated astrocytes, colored by their relative abundance from RCTD analysis that integrates *Visium* data¹⁸ with the single-cell

transcriptome atlas, shown for both adult and aged samples. (d) Display of the distribution of interactions among reactive oligodendrocytes and DAM, reactive oligodendrocytes and activated astrocytes, and DAM and activated astrocyte utilizing *Visium* data¹⁸ with the single-cell transcriptome atlas, shown for both adult and aged samples. (e) Histogram illustrating the null distribution of beads with both reactive oligodendrocytes and activated astrocytes assuming random distribution, with a dashed line marking the observed number. (f) Heatmap showing the normalized gene expression in DAM, reactive oligodendrocytes, activated astrocytes, and the corresponding main cell types.



Extended Data Fig. 9 | Heatmap of canonical marker gene expression across cell subtypes. Heatmap of canonical marker gene expression across cell subtypes. Panels (a–g) display representative marker expression patterns across distinct cell populations.



Extended Data Fig. 10 | IRISeq Immunodeficiency brain quality control analysis. a. Number of beads across sections, and replicates. **b.** Box and whisker plot demonstrating the UMI distribution across all the lymphocyte deficiency

dataset. **c.** Number of UMI's per receiver bead across replicates. **d.** UMI distribution across the annotated brain regions. **e.** Heatmap depicting upregulated genes across both mutants.

Reporting Summary

Nature Portfolio wishes to improve the reproducibility of the work that we publish. This form provides structure for consistency and transparency in reporting. For further information on Nature Portfolio policies, see our [Editorial Policies](#) and the [Editorial Policy Checklist](#).

Statistics

For all statistical analyses, confirm that the following items are present in the figure legend, table legend, main text, or Methods section.

n/a | Confirmed

- The exact sample size (n) for each experimental group/condition, given as a discrete number and unit of measurement
- A statement on whether measurements were taken from distinct samples or whether the same sample was measured repeatedly
- The statistical test(s) used AND whether they are one- or two-sided
Only common tests should be described solely by name; describe more complex techniques in the Methods section.
- A description of all covariates tested
- A description of any assumptions or corrections, such as tests of normality and adjustment for multiple comparisons
- A full description of the statistical parameters including central tendency (e.g. means) or other basic estimates (e.g. regression coefficient) AND variation (e.g. standard deviation) or associated estimates of uncertainty (e.g. confidence intervals)
- For null hypothesis testing, the test statistic (e.g. F , t , r) with confidence intervals, effect sizes, degrees of freedom and P value noted
Give P values as exact values whenever suitable.
- For Bayesian analysis, information on the choice of priors and Markov chain Monte Carlo settings
- For hierarchical and complex designs, identification of the appropriate level for tests and full reporting of outcomes
- Estimates of effect sizes (e.g. Cohen's d , Pearson's r), indicating how they were calculated

Our web collection on [statistics for biologists](#) contains articles on many of the points above.

Software and code

Policy information about [availability of computer code](#)

Data collection

Data were collected using Illumina NextSeq 6000 and NovaSeq sequencing platforms. Initial data processing, including base calling and demultiplexing, was performed using standard Illumina software. Downstream preprocessing and quality control were conducted using custom scripts in Python and R.

Data analysis

All data analysis was performed using custom and open-source code written in Python (v3.19) and R (v4.0.3). Key packages included Scanpy (v1.9), Seurat (v4.1.1), ggplot2 (v3.4), pandas (v1.4.3), and NumPy (v1.22.4). Custom scripts will all be available on <https://github.com/JunyueCaoLab>. The code is available with github web-link (:<https://github.com/AbdulAbdulRU/IRISeq>)

For manuscripts utilizing custom algorithms or software that are central to the research but not yet described in published literature, software must be made available to editors and reviewers. We strongly encourage code deposition in a community repository (e.g. GitHub). See the Nature Portfolio [guidelines for submitting code & software](#) for further information.

Data

Policy information about [availability of data](#)

All manuscripts must include a [data availability statement](#). This statement should provide the following information, where applicable:

- Accession codes, unique identifiers, or web links for publicly available datasets
- A description of any restrictions on data availability
- For clinical datasets or third party data, please ensure that the statement adheres to our [policy](#)

A detailed protocol of the IRISseq platform is outlined in supplementary note 1. Raw FASTQ files, processed count matrices, cell metadata, and gene metadata can be downloaded from NCBI GEO under accession number GSE270383 (GEO reviewer token: izwrekiyffwjhyp)

Research involving human participants, their data, or biological material

Policy information about studies with [human participants or human data](#). See also policy information about [sex, gender \(identity/presentation\), and sexual orientation](#) and [race, ethnicity and racism](#).

Reporting on sex and gender	All animals used in this study were female mice, across all age groups and genotypes, including mutant and control groups. Sex was determined based on biological characteristics at the time of animal acquisition. This information is detailed in Table 2. No sex-based comparative analyses were performed, as only one sex was included in the study.
Reporting on race, ethnicity, or other socially relevant groupings	N/A
Population characteristics	N/A
Recruitment	N/A
Ethics oversight	All animal procedures complied with institutional, state, and federal regulations, and were approved under IACUC protocols 21049 and 20047

Note that full information on the approval of the study protocol must also be provided in the manuscript.

Field-specific reporting

Please select the one below that is the best fit for your research. If you are not sure, read the appropriate sections before making your selection.

Life sciences Behavioural & social sciences Ecological, evolutionary & environmental sciences

For a reference copy of the document with all sections, see [nature.com/documents/nr-reporting-summary-flat.pdf](https://www.nature.com/documents/nr-reporting-summary-flat.pdf)

Life sciences study design

All studies must disclose on these points even when the disclosure is negative.

Sample size	Sample sizes were determined based on standard practice in transcriptomic studies, balancing biological variability, statistical power, and resource constraints. For each experimental comparison (mutant vs. wild-type and adult vs. aged), we included 3 biological replicates per group, totaling 9 samples for mutant analysis (WT, RAG1, PRKDC) and 6 for aging analysis (adult, aged). A sample size of 3 per group is commonly accepted in bulk and spatial transcriptomics studies to capture inter-individual variability while maintaining feasibility for high-throughput sequencing and downstream analyses. This sample size has been shown to be sufficient to identify robust and reproducible gene expression differences in similar contexts.
Data exclusions	No data was excluded
Replication	Reproducibility was evaluated using independent biological replicates and repeated analyses with the same predefined experimental and computational procedures. The main findings were consistently observed across replicate samples and experimental conditions, and/or genotypes. No results presented in this study were found to be irreproducible.
Randomization	Not relevant to this study, as each group cohort were pre assigned based on genotype and/or age group.
Blinding	Blinding was not relevant to study as each group was assigned prior to data collection.

Reporting for specific materials, systems and methods

We require information from authors about some types of materials, experimental systems and methods used in many studies. Here, indicate whether each material, system or method listed is relevant to your study. If you are not sure if a list item applies to your research, read the appropriate section before selecting a response.

Materials & experimental systems

- n/a | Involved in the study
- Antibodies
- Eukaryotic cell lines
- Palaeontology and archaeology
- Animals and other organisms
- Clinical data
- Dual use research of concern
- Plants

Methods

- n/a | Involved in the study
- ChIP-seq
- Flow cytometry
- MRI-based neuroimaging

Animals and other research organisms

Policy information about [studies involving animals](#); [ARRIVE guidelines](#) recommended for reporting animal research, and [Sex and Gender in Research](#)

Laboratory animals	C57BL/6 wild-type mice, B6.129S7-Rag1tm1Mom/J and B6.Cg-Prkdcscid/SzJ were acquired from the Jackson Laboratory and the National Institute on Aging colony at Charles River. Mice were housed under a 12-h light/12-h dark cycle in a pathogen-free, temperature- and humidity-controlled animal facility, with food and water provided ad libitum. Wild-type mice used for the aging studies were obtained from the National Institute on Aging (NIA) aged rodent colony. Immunodeficient mice were obtained from The Jackson Laboratory and included B6.129S7-Rag1 ^{tm1Mom} /J and B6.Cg-Prkdc ^{scid} /SzJ.
Wild animals	No wild animals were involved
Reporting on sex	All experiments were conducted using female mice across all age groups and genotypes. Sex was considered in the study design to control for sex-based variability. As only one sex was used, sex-based analyses were not performed. This information is detailed in Table S2.
Field-collected samples	No field-collected samples
Ethics oversight	All animal procedures complied with institutional, state, and federal regulations, and were approved under IACUC protocols 21049 and 20047. In all studies, we adhere to the recommendations for animal use and welfare, as outlined by Rockefeller University, the Comparative Bioscience Center, and the guidelines established by the NIH. The Federal Animal Welfare Assurance number for Rockefeller University is A3081.

Note that full information on the approval of the study protocol must also be provided in the manuscript.

Plants

Seed stocks	<i>Report on the source of all seed stocks or other plant material used. If applicable, state the seed stock centre and catalogue number. If plant specimens were collected from the field, describe the collection location, date and sampling procedures.</i>
Novel plant genotypes	<i>Describe the methods by which all novel plant genotypes were produced. This includes those generated by transgenic approaches, gene editing, chemical/radiation-based mutagenesis and hybridization. For transgenic lines, describe the transformation method, the number of independent lines analyzed and the generation upon which experiments were performed. For gene-edited lines, describe the editor used, the endogenous sequence targeted for editing, the targeting guide RNA sequence (if applicable) and how the editor was applied.</i>
Authentication	<i>Describe any authentication procedures for each seed stock used or novel genotype generated. Describe any experiments used to assess the effect of a mutation and, where applicable, how potential secondary effects (e.g. second site T-DNA insertions, mosaicism, off-target gene editing) were examined.</i>